Journal of Asian Earth Sciences 281 (2025) 106504

Contents lists available at ScienceDirect

Journal of Asian Earth Sciences

journal homepage: www.elsevier.com/locate/jseaes

Full length article

Origin of Late Triassic lamprophyres in the western Yanshan Tectonic Belt related to destruction of the North China Craton: Geochronological and geochemical constraints

Zhuang Li [a,b,*], Guochun Zhao [c,d], Bin Chen [e], Mingshuo Qin [a]

[a] College of Geosciences, China University of Petroleum (Beijing), Beijing 102249, PR China
[b] College of Carbon Neutral Energy, China University of Petroleum (Beijing), Beijing 102249, PR China
[c] State Key Laboratory of Continental Dynamics, Department of Geology, Northwest University, Xi'an 710069, PR China
[d] Department of Earth Sciences, The University of Hong Kong, Hong Kong, PR China
[e] Department of Earth and Space Sciences, Southern University of Science and Technology, Shenzhen 518055, PR China

ARTICLE INFO

Keywords:
Lamprophyre
Late Triassic
Onset of craton destruction
Upwelling of the asthenosphere
North China Craton

ABSTRACT

Lamprophyres, ultrapotassic igneous rocks generally derived from the melting of enriched subcontinental lithospheric mantle, typically form in extensional tectonic settings and are associated with coeval transcrustal processes. The genesis of lamprophyres provides insights into the generation, storage, and emplacement of lamprophyric magmas, and further constrains the nature of mantle sources. However, the origin of lamprophyres remains enigmatic and requires further investigation. The Late Triassic lamprophyres along the western Yanshan Tectonic Belt of the northern North China Craton (NCC) offer a key opportunity to understand the tectonic evolution of this region, particularly their relationship with the onset of craton destruction. Here we report the results of an integrated geochronological and geochemical study of Late Triassic lamprophyres and quartz monzonite porphyries in Beijing on the western Yanshan Tectonic Belt. U–Pb zircon dating using LA–ICP–MS reveals that the lamprophyres and quartz monzonite porphyries were emplaced contemporaneously during *ca.* 235–220 Ma, marking a Late Triassic magmatic event in the northern NCC. The Late Triassic lamprophyre and quartz monzonite porphyry sills are enriched in large ion lithophile elements (LILEs) and light rare earth elements (LREEs) but are depleted in high field strength elements (HFSEs), exhibiting arc-like geochemical characteristics. They also display high MgO and total alkali concentrations with low silica contents. Unradiogenic whole-rock Nd and Hf isotope compositions [($\varepsilon_{Nd}(t) = -11.3$ to -10.8) and ($\varepsilon_{Hf}(t) = -16.3$ to -12.5)] indicate that the magmas of the Triassic suite were likely derived from an enriched lithospheric mantle source, followed by fractional crystallization of ferromagnesian phases and minor crustal assimilation. Geochemical modeling suggests that the parental magma of the lamprophyres was generated through a low degree (<5 %) partial melting of spinel–garnet lherzolites. These results suggest that the investigated rocks originated from a subcontinental lithospheric mantle enriched by fluid and/or melt metasomatism, likely during subduction of the Paleo-Asian oceanic plate beneath the NCC. Radiogenic zircon Hf isotope compositions [e.g., $\varepsilon_{Hf}(t) = 6.4$ to 8.9] of the Late Triassic lamprophyres point to the involvement of a depleted mantle source. The upwelling of the asthenosphere, triggered by intensive intra-continental extension during the Triassic, likely provided the heat required to melt the enriched subcontinental lithosphere beneath the NCC. This Late Triassic interaction between the asthenosphere and the lithospheric mantle marks the onset of NCC destruction and contributed to its thermo-mechanical erosion.

1. Introduction

Archean–Paleoproterozoic cratons are stable tectonic units on Earth, characterized by a lack or rarity of post-Paleoproterozoic intensive tectonic or volcano-intrusive thermal activities compared to younger mobile and/or orogenic belts (Zhu et al., 2012; Wu et al., 2019). Generally, the subcontinental lithospheric mantle beneath cratons is thick, cold, low-density, refractory and anhydrous (Hirth et al., 2000;

* Corresponding author.
E-mail address: lizhuangcc@pku.edu.cn (Z. Li).

https://doi.org/10.1016/j.jseaes.2025.106504
Received 8 August 2024; Received in revised form 7 January 2025; Accepted 26 January 2025
Available online 31 January 2025

Jordan, 1975). However, not all cratons remain stable indefinitely, as exemplified by the Eastern Block of the North China Craton (NCC) (Carlson et al., 2005; Griffin et al., 1998; Menzies et al., 1993, 2007; Wu et al., 2003, 2006a, 2019; Xu, 2001), and the western Wyoming Craton (Ducea and Saleeby, 1988; Lee et al., 2000; Manley et al., 2000). These cratons are characterized by intensive felsic magmatism and related gold mineralization (Wang and Mo, 1996; Yang et al., 2003), extensional tectonics forming metamorphic core complexes, the development of extensional sedimentary basins (Yang et al., 2007a), and the exhumation of deep-seated rocks (Yang et al., 2008), ultimately leading to craton destruction or decratonization (Wu et al., 2019). Lithospheric thinning has long been regarded as a key indicator of craton destruction. The NCC is considered unique among Archean cratons due to its lithosphere undergoing significant thinning during the Mesozoic (e.g., Wang et al., 2021). Geochemical and geophysical data from ancient cratons, such as the Indian, Siberian, Brazilian, Yilgarn, Tanzanian, and North Atlantic Cratons, indicate lithospheric thinning or the removal of their lower domains without resulting in craton destruction (Griffin et al., 1998, 1999; Howarth et al., 2014; Read et al., 2004; Tappe et al., 2007). Evidence for lithospheric removal is provided by ancient diamond-bearing kimberlites and Cenozoic basalts or mantle and crustal xenoliths, which reveal that the thick and cold ancient lithospheric mantle had been converted into a thin and hot lithospheric mantle. This transformation occurred without significant magmatic, tectonic, or earthquake activity (Wu et al., 2019). Thus, lithospheric thinning fades into insignificance compared with the switch in the geophysical and geochemical properties of the lithospheric mantle that witnessed craton destruction. A hallmark of craton destruction is the switch in the mantle source region from ancient enriched lithospheric mantle to juvenile and depleted asthenospheric mantle (Menzies et al., 2007; Wu et al., 2006a; Xu et al., 2009; Yang and Wu, 2009; Yang et al., 2008). The upwelling of convective asthenosphere modifies the thermal structure of the lithosphere (Xu et al., 2009, 2018), leading to the loss of ancient lithospheric mantle beneath continents, triggering intensive crust-derived

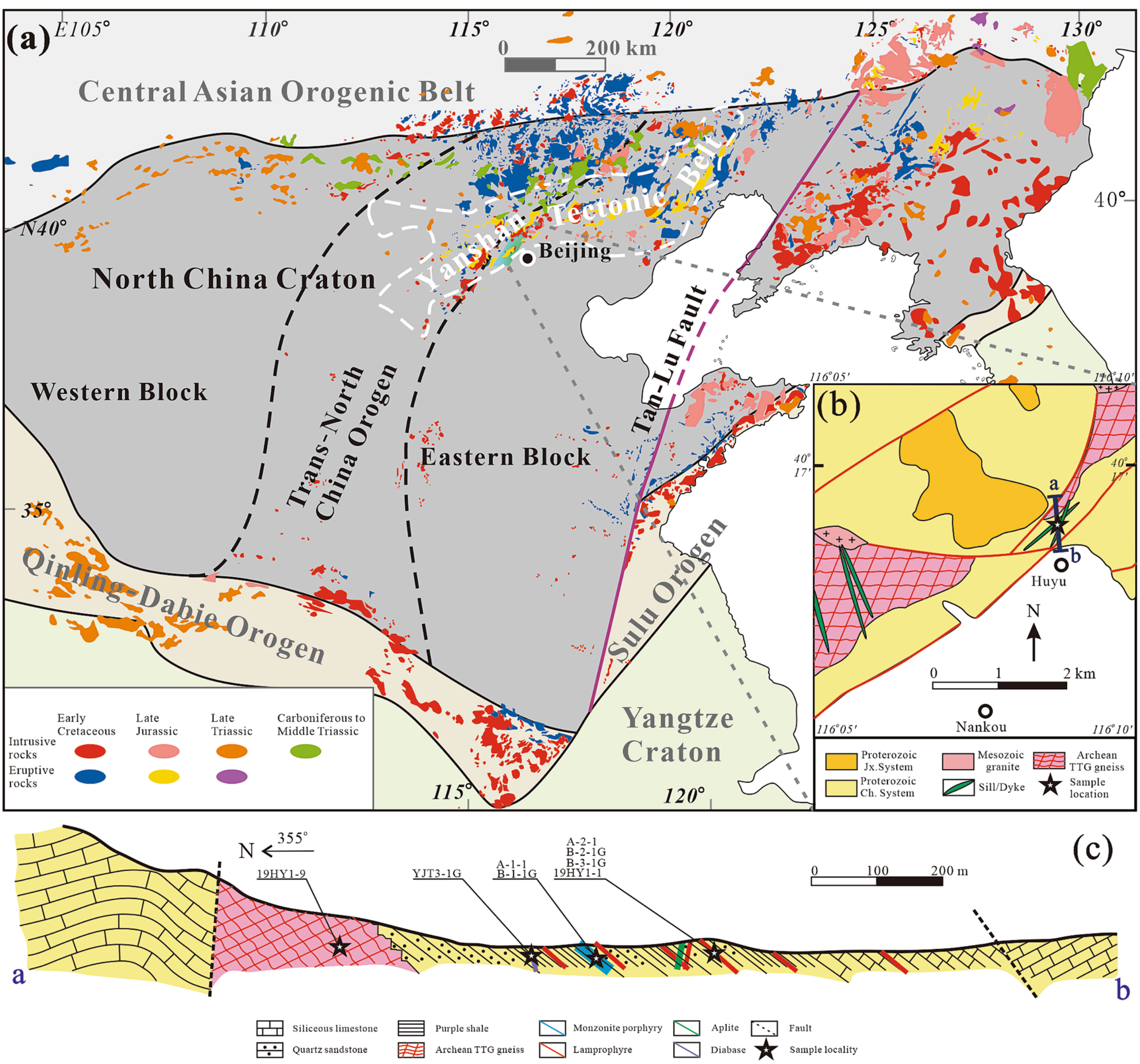

Fig. 1. (a) Subdivision of the NCC in the early Precambrian and distribution of Late Paleozoic to Mesozoic igneous rocks (after Wu et al., 2019; Zhao et al., 2005; Zhai and Santosh, 2013; Zhao and Zhai, 2013). (b) Geological map of northwestern Beijing, northern NCC. (c) Geological section along the northwestern Beijing (Ji et al., 2017).

magmatism, and causing deformation of crustal rocks (Wu et al., 2008, 2019).

Regional synthesis indicates three episodes of voluminous Mesozoic magmatism in the NCC (Fig. 1a): Triassic (234–206 Ma), Jurassic (200–145 Ma), and Early Cretaceous (145–110 Ma) (Wu et al., 2019). The majority of Triassic magmatism is characterized by an east–west-trending alkaline igneous rock belt along the northern and southern margins with some exposures in the eastern part (Yang and Wu, 2009; Yang et al., 2007b; Zhang et al., 2014). Jurassic igneous rocks are primarily distributed in the eastern NCC (Yang et al., 2007c), while Early Cretaceous magmatism is widespread across the entire NCC (Yang et al., 2003; Wu et al., 2019). All three magmatic episodes are dominated by intermediate to acidic rocks, with minor mafic components (Yang et al., 2008) (Fig. 1a). The study area has been extensively researched for several decades (e.g., Gao et al., 2004; Liu et al., 2019; Wu et al., 2019; Xu, 2001; Yang and Wu, 2009; Yang et al., 2008). However, the magmatic and tectonic evolution of the region remains unclear. This study aims to elucidate the processes and mechanisms of craton destruction. The complexity in the origin of intermediate–acidic rocks and the potential crustal contributions has hindered the application of these Mesozoic crust-derived rocks in probing deep mantle processes (Wu et al., 2007; Yang et al., 2004). In contrast, mantle-derived mafic magmatism has been extensively used as a proxy for understanding the geodynamic processes responsible for NCC destruction, characterizing the nature of the mantle source, and exploring the relationship between Mesozoic magmatism and lithospheric mantle evolution (Yang and Wu, 2009). Two contrasting Mesozoic magmatic suites were recently identified in northwestern Beijing of the western Yanshan Tectonic Belt of the NCC: the Late Triassic lamprophyre and quartz monzonite porphyry sills, and the Early Cretaceous diabase dykes. Chronologically, the former corresponds to the initial stage of craton destruction, and the latter to the peak stage (Yang et al., 2007b; Yang and Wu, 2009; Zhang et al., 2009a). Lamprophyres generally form in extensional tectonic settings and record transcrustal or crust–mantle interactions, though their relationship with the mantle source remains unresolved. Lamprophyres are widely accepted to form by low-degree melting of enriched subcontinental lithospheric mantle (Fowler and Henney, 1996; Gibson et al., 1995; McKenzie, 1989; Thompson et al., 1990). Consequently, these rocks are key agents for understanding enrichment and depletion processes, as well as the origin of the enriched component in the subcontinental lithospheric mantle. Additional components involved in their formation include a mantle source assimilated with crustal material, an extremely depleted mantle, and/or a convective mantle (Aghazadeh et al., 2015; Prelević et al., 2004, 2008). Further research is required to unravel key questions surrounding the origin of lamprophyres and their relationship with the onset of craton destruction. In this contribution, systematic investigations of the Late Triassic lamprophyre and quartz monzonite porphyry sills are conducted using whole-rock major and trace element and Hf–Nd isotopic data, along with zircon U–Pb–Hf isotopic analyses. These data provide rare opportunities and robust evidence to elucidate the petrogenesis of Late Triassic lamprophyres and the Mesozoic mantle source. The study offers a window into Mesozoic mantle processes and further clarifies their linkage to the onset of craton destruction.

2. Geological setting, and field and petrographic observations

The NCC, the largest craton in China, covering an area of approximately 300 000 km^2, is bounded by the Paleozoic Central Asian Orogenic Belt to the north and the Kunlun–Qinling–Dabie–Su–Lu Orogenic Belt to the south (Zhao and Zhai, 2013) (Fig. 1a). It is one of the oldest continental nuclei on Earth, with 3.8 Ga trondhjemites (Liu et al., 2008; Song et al., 1996; Wan et al., 2005, 2012) and zircons dated to 4.0 Ga (Diwu et al., 2013; Li et al., 2016b; Li and Chen, 2019). The NCC is subdivided into the Eastern and Western Blocks, which are amalgamated along the Trans-North China Orogen (Zhai and Santosh, 2011; Zhao and Zhai, 2013; Zhao and Kröner, 2007) (Fig. 1a). The Eastern Block comprises the Archean Longgang Block in the north, the Archean Nangrim Block in the south, and the intervening Paleoproterozoic Jiaoliao Mobile Belt or Jiao–Liao–Ji Belt (Li et al., 2016a, 2019; Zhao and Zhai, 2013; Zhao et al., 2005). Northwestern Beijing, the primary study area of this contribution, is located on the northern margin of the Eastern Block, near the Trans-North China Orogen (Ji et al., 2017; Ren et al., 2011) (Fig. 1a). The Archean basement in this region primarily consists of *ca.* 2.5 Ga granitoid gneisses (tonalite–-trondhjemite–granodiorite, hereafter referred to as TTG) and supracrustal remnants (e.g., mafic granulites and amphibolites; Zhai and Santosh, 2013; Zhao and Zhai, 2013). These basement rocks are unconformably overlain by Mesoproterozoic–Neoproterozoic and Cambrian–Ordovician marine clastic and carbonate platformal sediments. During the Middle to Late Ordovician, the NCC experienced uplift, resulting in a significant sedimentation gap until the Middle Carboniferous. Subsequently, fluvial and deltaic sediments were deposited from the Middle Carboniferous to the Triassic. These strata also include local exposures of Jurassic–Cretaceous and younger volcano-sedimentary successions (Fig. 1b). The Eastern Block remained relatively quiescent for an extended period prior to the Early Triassic, with no regional angular unconformities between the younger cover sequences and only minor eruptions of anorogenic and deep mantle-derived rocks such as carbonatite and kimberlite (*ca.* 460 ~ 470 Ma; Yang et al., 2009; Zhang and Yang, 2007), along with related igneous rocks (Zhang et al., 2009b) (Fig. 1a). During the Late Mesozoic, the NCC underwent significant remobilization, characterized by intense deformation (e.g., Davis et al., 1998, 2001; Zhao, 1990; Zhang et al., 2011; Zheng et al., 2000), widespread magmatism (e.g., Deng et al., 2007; Wan and Zhao, 2012; Wu et al., 2005a,b, 2006a), and metallic mineralization (e.g., Li and Santosh, 2014; Mao et al., 2003, 2005; Yang et al., 2003; Zhai and Santosh, 2013). These tectonic events broadly correspond to the destruction of the NCC. The widely distributed Mesozoic rocks in the Eastern Block can be divided into several stages of magmatism, including the Triassic, Jurassic, and Early Cretaceous (Fig. 1a). Late Triassic magmatic rocks are abundant along the northern margin, represented by the Yinshan and Yanshan Tectonic Belts, as well as the eastern margin, including the Liaodong and the southern Yanbian–Liaobei area of the NCC (Fig. 1a).

The basement in northwestern Beijing is primarily composed of Late Neoarchean TTG gneisses (Fig. 1c; Fig. 2a and b), which are unconformably overlain by a thick sequence of Mesoproterozoic Changchengian (Ch.) and Jixianian (Jx.) systems comprising quartz sandstone, shale, and limestone (Fig. 1c; Fig. 2c and d). The study area is located in the southernmost part of the Triassic magmatic belt along the western Yanshan Tectonic Belt of the northern NCC. Mesozoic magmatic suites, in the form of sills or dykes have been identified within the Ch. System (Fig. 1c; Fig. 2e–l), including the Late Triassic lamprophyre and quartz monzonite porphyry sills (235–220 Ma; Fig. 2e and g), aplite dykes (206 Ma; Ji et al., 2017) (Fig. 2i), and Early Cretaceous diabase dykes (128 Ma; Fig. 2k). The lamprophyres are usually dark in color, exhibit porphyritic textures, and contain phenocrysts (35 %–40 %) of hornblende and biotite, with the latter partially altered to chlorite. Hornblende occurs as subhedral massive or needle-like crystals, while biotite forms subhedral or irregular flakes. The groundmass mainly consists of alkali feldspar, biotite, and pyroxene (Fig. 2f). The quartz monzonite porphyry samples are usually gray in color, exhibit porphyritic textures, and contain phenocrysts (15 %–20 %) of plagioclase and alkali feldspar within a groundmass of plagioclase, alkali feldspar, and muscovite (Fig. 2h). The aplite dykes are typically white and composed of quartz, alkali feldspar, and minor plagioclase, with characteristic aplitic textures (Fig. 2j).

3. Analytical methods

We have carried out LA–ICP–MS U–Pb dating, trace elements, and LA–MC–ICP–MS Hf isotope analyses on zircon grains, and major and

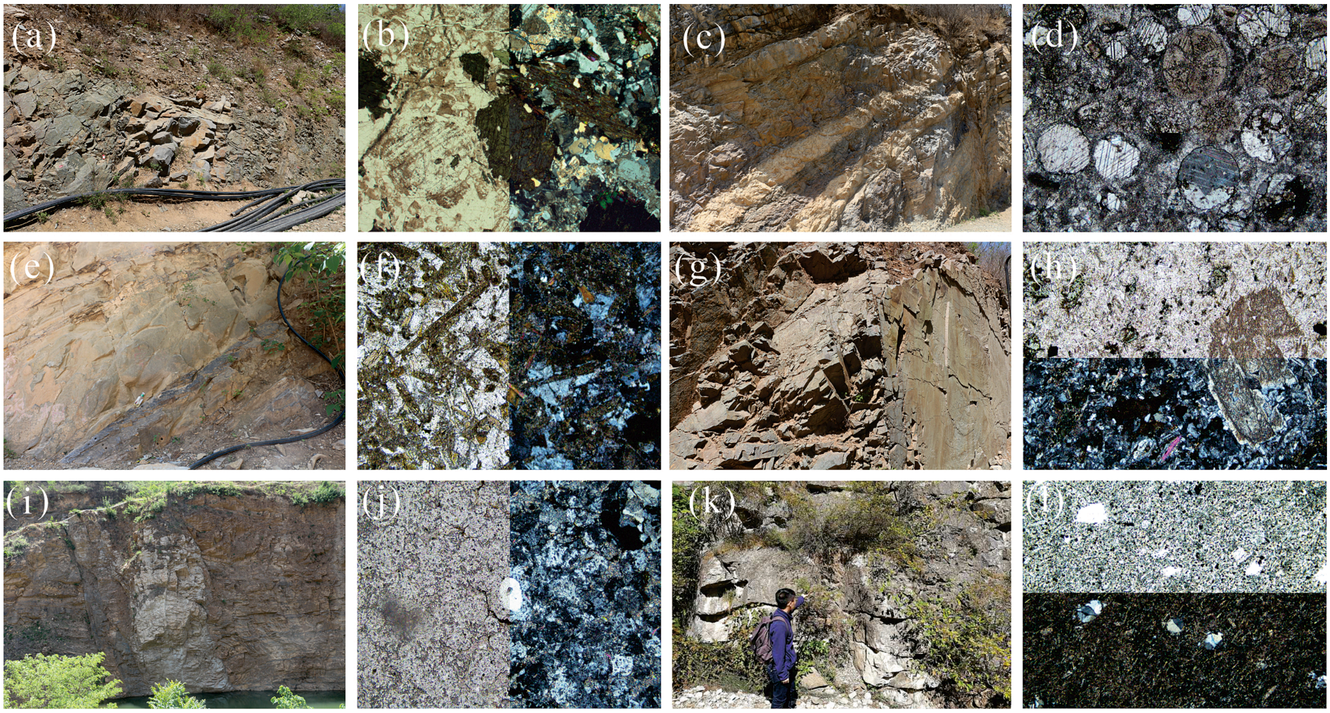

Fig. 2. Photographs of the outcrops and photomicrographs of the representative samples in northwestern Beijing, northern NCC.

trace element, and Nd–Hf isotope analyses on whole-rock of the Late Triassic lamprophyres and quartz monzonite porphyries, and their country rocks in northwestern Beijing, northern NCC.

3.1. Zircon U–Pb age determinations and isotopic analysis

Zircon grains from the Late Triassic lamprophyre and quartz monzonite porphyry sills, the Early Cretaceous diabase dykes, and Neoarchean granodioritic gneisses were extracted using heavy-liquid separation and magnetic extraction techniques followed by hand-picking under a binocular microscope. Zircons were placed in an epoxy mount, polished, and then vacuum-coated with a layer of 50-nm high-purity gold. Cathodoluminescence (CL) images of the zircons were collected on a HTACHI S-3000N scanning electron microscope with a GATAN Chroma CL probe at the Chengpu geological Testing Co., Ltd, Langfang, China.

Zircon grains were dated by LA–ICP–MS at the Chengpu geological Testing Co., Ltd, Langfang, China. A 193 nm excimer laser was focused on the surfaces of the zircon grains at an energy density of 10 J/cm^2. The diameter and repetition rate of the laser beam were 30 μm and 5 Hz, respectively. Helium was used as a carrier gas to transport the ablated aerosol to the LA–ICP–MS instrument. Each data set, consisting of eight sample analyses, was bracketed with analyses of zircon standards 91,500 and Temora-2, and the glass standard NIST612. Each spot analysis consisted of a *ca.* 5 s acquisition of background and 45 s of the sample. Isotopic ratios of ^{207}Pb/^{206}Pb, ^{206}Pb/^{238}U, ^{207}U/^{235}U, and ^{208}Pb/^{232}Th were corrected for instrumental bias and elemental fractionation effects using the analyses of zircon standard 91500. Trace element concentrations and U–Pb isotopic compositions were calculated using the GLITTER v. 4.4.1 software, and subsequently corrected using ^{29}Si as an internal standard and NIST612 as an external standard. Common Pb was corrected based on the method described by Andersen (2002). Weighted mean U–Pb ages and concordia plots were processed using the Isoplot/Ex v. 2.49 programs, with uncertainties quoted at the 2σ and 95 % confidence levels (Ludwig, 2003). Details of the analytical procedures and data processing methods can be found in Liu et al. (2008) and Song et al. (2010).

3.2. Zircon Hf isotope analysis

In-situ Hf isotope analyses on zircons from the Late Triassic lamprophyre and quartz monzonite porphyry sills were performed using a New Wave UP213 laser coupled to a Neptune multi-collector ICP–MS (LA–MC–ICP–MS) at the Wuhan Sample Solution Analytical Technology Co., Ltd, Wuhan, China. Details of the instrumental conditions and data acquisition procedures have been elucidated by Hou et al. (2007) and Wu et al. (2006b). During the analyses, a spot size of 40 μm and laser repetition rate of 6 Hz at 100 mJ were chosen, and raw count rates were collected for ^{172}Yb, ^{173}Yb, ^{175}Lu, ^{176}(Hf + Yb + Lu), ^{177}Hf, ^{178}Hf, ^{179}Hf, ^{180}Hf, and ^{182}W. Ablated materials were transported from the laser ablation cell using Helium as a carrier gas, and then combined with Argon in a mixing chamber before being introduced to the ICP–MS plasma. ^{176}Lu and ^{176}Yb isobaric interferences with ^{176}Hf readings were corrected by applying ^{176}Lu/^{175}Lu = 0.02658 and ^{176}Yb/^{173}Yb = 0.796218, respectively (Chu et al., 2002). Instrumental mass bias was corrected by normalizing Yb isotope ratios to ^{172}Yb/^{173}Yb = 1.35274 (Chu et al., 2002; Wu et al., 2006b) and Hf isotope ratios to ^{179}Hf/^{177}Hf = 0.7325 based on the exponential mass fractionation law. Detailed instrumental settings and descriptions of the analytical technique can be found in Chu et al. (2002) and Hou et al. (2007). The ^{176}Hf/^{177}Hf ratio of the standard zircon 91500, obtained during our analyses, was 0.282295 ± 0.000020 (2σ). Measured ^{176}Hf/^{177}Hf and ^{176}Lu/^{177}Hf ratios were used to calculate initial ^{176}Hf/^{177}Hf ratios, with the decay constant of ^{176}Lu as 1.865 × 10^{-11} year^{-1} (Scherer et al., 2001). The present-day chondritic ratios of ^{176}Hf/^{177}Hf = 0.282772 and ^{176}Lu/^{177}Hf = 0.0332 (Blichert-Toft and Albarède, 1997) were adopted to calculate the ε_{Hf}(t) values. All Hf isotope data were reported with 2σ error. In addition, the ε_{Hf}, T_{Hf}, T_{Hf2} and $f_{Lu/Hf}$ in this study were defined as follows:

$$\varepsilon_{Hf(0)} = \left(\frac{(^{176}Hf/^{177}Hf)_S}{(^{176}Hf/^{177}Hf)_{CHUR,0}} - 1\right) \times 10000 \quad (i)$$

$$\varepsilon_{\mathrm{Hf(t)}} = \left(\frac{(^{176}\mathrm{Hf}/^{177}\mathrm{Hf})_S - (^{176}\mathrm{Lu}/^{177}\mathrm{Hf})_S \times (e^{\lambda t} - 1)}{(^{176}\mathrm{Hf}/^{177}\mathrm{Hf})_{CHUR,0} - (^{176}\mathrm{Lu}/^{177}\mathrm{Hf})_{CHUR} \times (e^{\lambda t} - 1)} - 1 \right) \times 10000 \quad \text{(ii)}$$

$$T_{\mathrm{Hf}}(\mathrm{Ma}) = 1/\lambda \times \ln\left[1 + \frac{(^{176}\mathrm{Hf}/^{177}\mathrm{Hf})_S - (^{176}\mathrm{Hf}/^{177}\mathrm{Hf})_{DM}}{(^{176}\mathrm{Lu}/^{177}\mathrm{Hf})_S - (^{176}\mathrm{Lu}/^{177}\mathrm{Hf})_{DM}}\right] \quad \text{(iii)}$$

$$T_{\mathrm{Hf2}}(\mathrm{Ma}) = T_{\mathrm{Hf}} - (T_{\mathrm{Hf}} - t)\left(\frac{f_{CC} - f_S}{f_{CC} - f_{DM}}\right) \quad \text{(iv)}$$

$$f_{\mathrm{Lu/Hf}} = \frac{(^{176}\mathrm{Lu}/^{177}\mathrm{Hf})_S}{(^{176}\mathrm{Lu}/^{177}\mathrm{Hf})_{CHUR}} - 1 \quad \text{(v)}$$

where $(^{176}\mathrm{Lu}/^{177}\mathrm{Hf})_S$ and $(^{176}\mathrm{Hf}/^{177}\mathrm{Hf})_S$ were obtained from sample measurements, $(^{176}\mathrm{Lu}/^{177}\mathrm{Hf})_{\mathrm{CHUR}} = 0.0332$ and $(^{176}\mathrm{Hf}/^{177}\mathrm{Hf})_{\mathrm{CHUR,0}} = 0.282772$ (Blichert-Toft and Albarède, 1997); $(^{176}\mathrm{Lu}/^{177}\mathrm{Hf})_{\mathrm{DM}} = 0.0384$ and $(^{176}\mathrm{Hf}/^{177}\mathrm{Hf})_{\mathrm{DM}} = 0.28325$ (Griffin et al., 2000); t is the crystallization age of the zircon; and $\lambda = 1.867 \times 10^{-11}$ y^{-1} (Amelin, 2005). The T_{Hf} were calculated based on the measured $^{176}\mathrm{Lu}/^{177}\mathrm{Hf}$ and $^{176}\mathrm{Hf}/^{177}\mathrm{Hf}$ ratios with reference to depleted mantle from present-day measurements, $(^{176}\mathrm{Lu}/^{177}\mathrm{Hf})_{\mathrm{DM}} = 0.0384$ and $(^{176}\mathrm{Hf}/^{177}\mathrm{Hf})_{\mathrm{DM}} = 0.28325$ (Griffin et al., 2000). The T_{Hf2} were calculated using the initial $^{176}\mathrm{Lu}/^{177}\mathrm{Hf}$ value of the zircon, assuming a mean crustal value of 0.015 (Griffin et al., 2000).

3.3. Whole–rock major and trace element analyses

After removing the altered surfaces from rock samples, fresh parts were crushed in an agate mill to ~200 meshes. Whole-rock major and trace element analyses on powdered samples were performed at the Wuhan Sample Solution Analytical Technology Co., Ltd, Wuhan, the Geoanalytical Center of Nuclear Industry, Beijing, and Geological Laboratory Center of China University of Geosciences, Beijing, using X-ray fluorescence spectrometry (XRF) and ICP–MS, respectively. Analytical uncertainties were 1–3 % for major elements. For trace and rare earth element (REE) analyses, about 50 mg rock powders were dissolved using mixed acids ($HF/HClO_4$) in capped Savillex Teflon breakers at 120 °C for 6 days, and subsequently dried to wet salt and re-dissolved in 0.5 ml $HClO_4$. The solutions were then evaporated to wet salt at 140 °C and re-dissolved in 1 ml HNO_3 and 3 ml water for 24 h at 120 °C. The solutions were diluted in 2 % HNO_3 for analysis. The uncertainties based on the replicate analyses of internal standards were ±5 % for REE and ±5–10 % for trace elements. The analytical processes were followed after the methods described in Gao et al. (2010).

3.4. Whole-rock Nd–Hf isotope analysis

Nd isotopic measurements on whole-rock samples were performed on the MC–ICP–MS at the Wuhan Sample Solution Analytical Technology Co., Ltd, Wuhan, China. Sample dissolution was carried out using acid digestion (HNO_3 + HF) in a sealed Savillex beaker on a hot plate (80 °C). Sm and Nd were further purified using a second cation-exchange column, conditioned and cleaned with dilute HCl as described by Li and Chen (2014) and Li and Wei (2017). $^{143}\mathrm{Nd}/^{144}\mathrm{Nd}$ ratios were normalized to $^{146}\mathrm{Nd}/^{144}\mathrm{Nd} = 0.7219$ and adjusted to JMC Nd_2O_3 $^{143}\mathrm{Nd}/^{144}\mathrm{Nd} = 0.511122$. The uncertainty (2σ) in concentration measurement by isotope dilution is 0.2–0.5 % for Sm and Nd depending on their concentrations. Average procedural blanks were 50 pg for Sm and 50–100 pg for Nd. The decay constant used in age calculation was 0.00654 Ga^{-1} for ^{147}Sm.

Hf isotopic measurements were also performed at the Wuhan Sample Solution Analytical Technology Co., Ltd, Wuhan, China. The homogeneous mixtures of about 0.5 g of sample powders and 1.0 g of $Li_2B_4O_7$ were fused in Pt crucibles at 1250 °C for 15 min in a high-frequency furnace. Then, about 400 mg of the resulting glassy samples were dissolved in 2 N HCl. The Hf fraction was separated using a modified single-column separation procedure involving ion exchange with Ln-Spec resin. Detailed analytical procedures are reported in Li et al. (2006). The $^{176}\mathrm{Hf}/^{177}\mathrm{Hf}$ ratios were normalized to $^{179}\mathrm{Hf}/^{177}\mathrm{Hf} = 0.7325$, with the uncertainty (2σ) in concentration measurement by isotope dilution. The procedural blanks were 50 pg for Hf.

4. Results

4.1. Zircon U–Pb geochronology and trace elements

Representative CL images of the analyzed zircon grains, along with *in-situ* U–Pb ages, and U–Pb concordia diagrams, are shown in Figs. 3 and 4, respectively. The results of zircon U–Pb dating and trace element analyses are presented in Table 1. The red, green, and blue solid circles in Fig. 3 represent U–Pb dating sites corresponding to the magmatic, later-thermal-event and trapped domains of zircons, respectively.

4.1.1. Archean granodioritic gneiss

Zircon grains obtained from the Archean granodioritic gneiss sample (19HY1-9) are generally pale yellow to colorless, transparent, and mostly subhedral columnar, with long axes of 100–150 μm. Most grains exhibit core–rim structures in the CL images (Fig. 3a). Twenty spots were analyzed on 18 zircon grains and the results can be summarized into two categories: (i) Most cores are gray with either weak internal oscillatory zoning or striped absorption. These relic cores have high Th and U contents (Th = 197 ppm and U = 339 ppm on average) and high Th/U ratios (0.38–0.86, averaging 0.61; Table 1), indicating a typical magmatic origin (Belousova et al., 2002; Corfu et al., 2003; Hanchar and Rudnick, 1995; Hoskin and Black, 2000). Ten zircon analyses yield an upper intercept age of 2481 ± 20 Ma (mean square weighted deviation (MSWD) = 0.8), which is consistent with the $^{207}\mathrm{Pb}/^{206}\mathrm{Pb}$ weighted mean age of 2475 ± 13 Ma (MSWD = 2.8, n = 5) obtained from concordant or nearly concordant zircons (degree of discordance <10 %). We interpret the weighted mean $^{207}\mathrm{Pb}/^{206}\mathrm{Pb}$ age of approximately 2.5 Ga as the emplacement age (Fig. 4a). (ii) The gray rims exhibit sector zoning and share similar Th/U ratios with the magmatic cores mentioned above (0.45–0.69, averaging 0.54; Table 1). These rim domains may have formed during later tectono-thermal events, consistent with results reported from the nearby northern Liaoning Province (Li et al., 2019, 2021a,b, 2022). The core–rim boundaries are commonly serrated, indicating a history of dissolution (Andersson et al., 2002; Liu et al., 2012) (Fig. 3a). In contrast, the trapped zircon domains exhibit relatively low Th and U contents (Th = 76 ppm and U = 175 ppm on average) but high Th/U ratios (0.22–0.66, averaging 0.47; Table 1). Three zircon analyses yield an upper intercept age of 2714 ± 44 Ma (MSWD = 1.0), consistent with the $^{207}\mathrm{Pb}/^{206}\mathrm{Pb}$ weighted mean age of 2711 ± 27 Ma (MSWD = 4.4, n = 2) obtained from concordant or nearly concordant zircons (Fig. 4a). We interpret the weighted mean $^{207}\mathrm{Pb}/^{206}\mathrm{Pb}$ age of approximately 2.7 Ga as evidence of an Early Neoarchean tectono-thermal event, which has been reported from western Shandong Province of the NCC (Wan et al., 2011, 2012; Wu et al., 2013, 2014).

4.1.2. Late Triassic quartz monzonite porphyry

Zircon grains obtained from Late Triassic quartz monzonite porphyry samples (A-1-1 and B-1-1G) are generally pale yellow, transparent, and mostly euhedral prismatic crystals, with long axes of 80–150 μm. These grains can be subdivided into two types based on CL images and ages. In CL images, most grains (Type 1) appear gray with strong oscillatory zoning (Fig. 3b and c). These features, along with high Th and U contents (88–558 ppm and 224–631 ppm, respectively) and Th/U ratios (0.34–1.58) (Table 1), indicate a typical magmatic origin for these zircons (Baines et al., 2009; Hoskin, 2001; Koglin et al., 2009; Pupin, 1980). The remaining grains (Type 2) exhibit core–rim structures in CL images and yield older ages than Type 1 zircons. These grains commonly

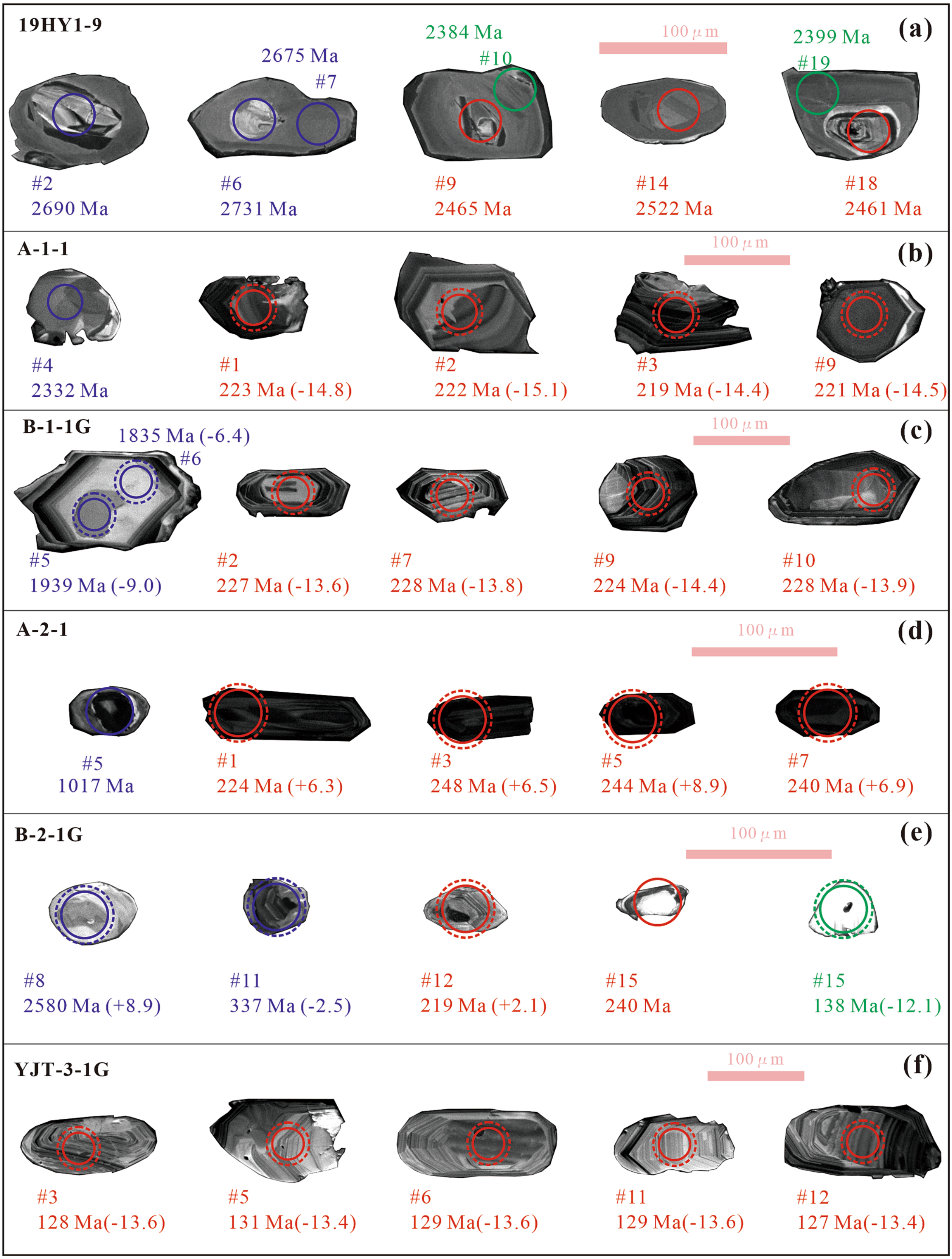

Fig. 3. CL images for representative zircons from Late Triassic lamprophyre and quartz monzonite porphyry sills, the Early Cretaceous diabase dykes, and Neoarchean granodioritic gneisses in northwestern Beijing. The red, green and blue solid circles represent U–Pb dating sites of the magmatic, later-thermal-event and trapped domains of zircons, respectively. The red and blue dashed circles represent Hf isotope sites of the magmatic and trapped domains of zircons, respectively. The numbers near the circle are the spot number, U–Pb age, and $\varepsilon_{Hf}(t)$ value in round bracket. (For interpretation of the references to color in this figure legend, the reader is referred to the web version of this article.)

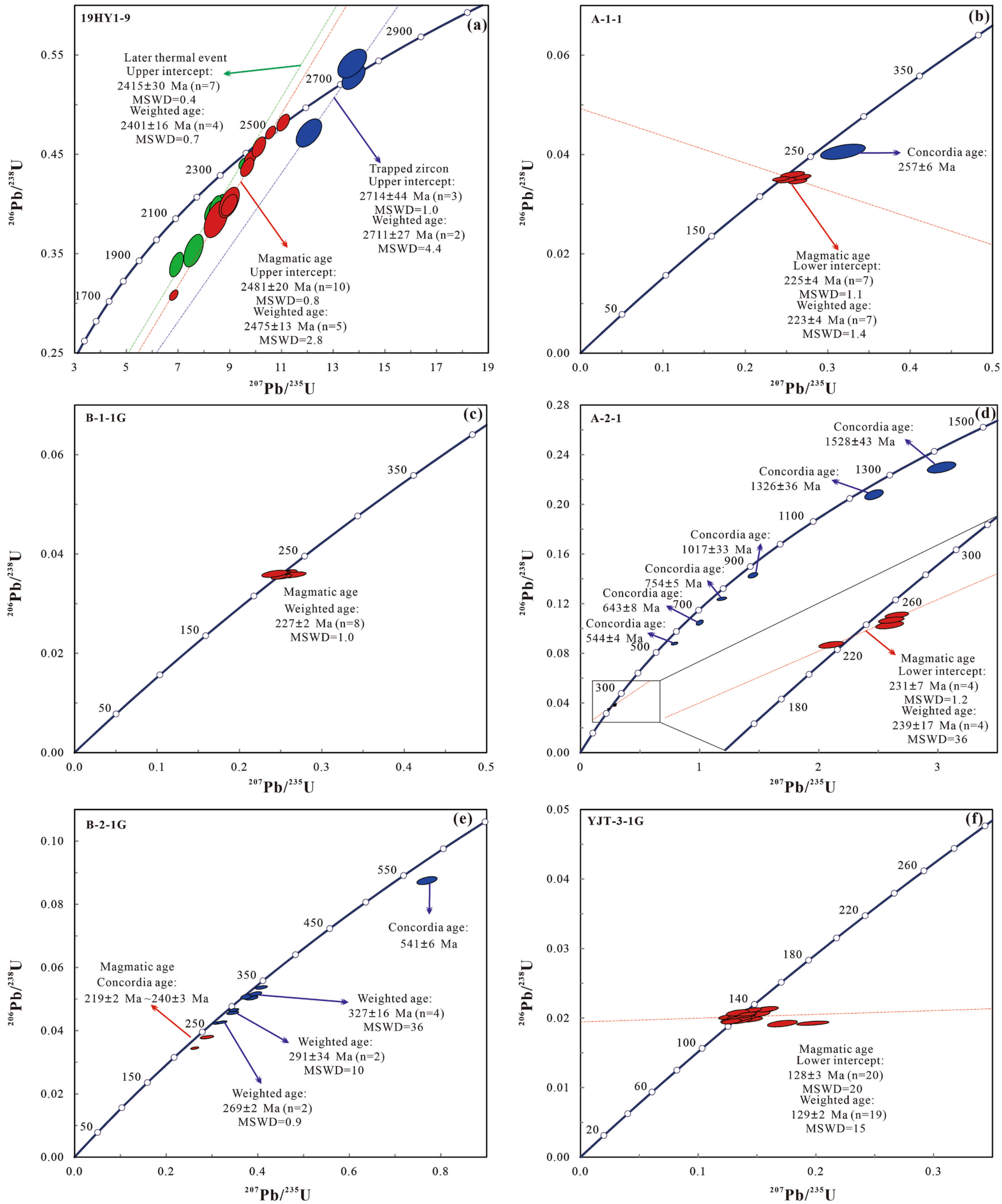

Fig. 4. U–Pb zircon concordia diagrams for Late Triassic lamprophyre and quartz monzonite porphyry sills, the Early Cretaceous diabase dykes, and Neoarchean granodioritic gneisses in northwestern Beijing, northern NCC.

have low Th and U contents (20–75 ppm and 34–524 ppm, respectively), and exhibit varied Th/U ratios (0.11–0.83). Seven Type 1 zircon analyses from Sample A-1–1 define an upper intercept age of 225 ± 4 Ma (MSWD = 1.1), consistent with the ^{206}Pb/^{238}U weighted mean age of 223 ± 4 Ma (MSWD = 1.4) obtained from all seven concordant zircons (Fig. 4b). Similarly, eight Type 1 zircon analyses from Sample B-1-1G also yield a ^{206}Pb/^{238}U weighted mean age of 227 ± 2 Ma (MSWD = 1.0) from all eight concordant zircons (Fig. 4c). We interpret the weighted mean ^{206}Pb/^{238}U age of Type 1 zircons (*ca.* 220–230 Ma) as the emplacement age of the Late Triassic quartz monzonite porphyry (Fig. 4b and c). The Type 2 domains are trapped zircons, exhibiting relatively complex internal structures, with varied ages ranging from the

Table 1
U–Pb dating and trace element composition of zircon.

Spot	Pb (Total) (ppm)	Pb (Common) (ppm)	Th (ppm)	U (ppm)	Th/U	Isotopic ratios $^{207}Pb/^{206}Pb$	1σ	$^{207}Pb/^{235}U$	1σ	$^{206}Pb/^{238}U$	1σ	Corrected ages (Ma) $^{207}Pb/^{206}Pb$	1σ	$^{207}Pb/^{235}U$	1σ	$^{206}Pb/^{238}U$	1σ	Disc (%)	Ti (ppm)	Temperature °C	La (ppm)	Ce (ppm)	Pr (ppm)	Nd (ppm)	Sm (ppm)	Eu (ppm)	Gd (ppm)	Tb (ppm)	Dy (ppm)	Ho (ppm)	Er (ppm)	Tm (ppm)	Yb (ppm)	Lu (ppm)
19HYI-9	Archean granodioritic gneiss																																	
	Magmatic zircon																																	
19HYI-9 - 01	175	0	171	267	0.64	0.1590	0.0017	9.7954	0.1557	0.4464	0.0053	2456	19	2416	15	2379	24	3.11	50.0	905	0.7	24.3	0.4	2.7	2.4	0.9	11.2	3.7	46.2	17.2	75.0	16.0	146.7	30.7
19HYI-9 - 09	183	1	180	268	0.67	0.1607	0.0022	9.6744	0.1710	0.4372	0.0061	2465	23	2404	16	2338	28	5.14	49.7	905	0.1	17.7	0.1	1.0	1.8	0.3	8.3	2.7	32.9	12.7	54.5	11.9	111.4	23.5
19HYI-9 - 11	249	0	239	365	0.65	0.1605	0.0015	10.1276	0.1730	0.4576	0.0067	2461	11	2446	16	2429	30	1.32	17.9	794	0.3	21.9	0.1	0.9	2.1	0.5	8.9	3.3	37.7	14.2	64.8	13.9	127.6	26.8
19HYI-9 - 14	161	5	164	218	0.75	0.1664	0.0016	11.0679	0.1607	0.4821	0.0056	2522	16	2529	14	2536	24	-0.57	17.4	792	0.0	20.2	0.1	1.2	2.0	0.5	11.4	4.1	46.7	18.1	79.5	17.2	155.0	31.8
19HYI-9 - 17	236	1	250	326	0.77	0.1623	0.0013	10.5812	0.1286	0.4721	0.0042	2480	14	2487	11	2493	19	-0.51	14.0	771	0.0	20.9	0.1	1.0	2.1	0.5	12.1	4.1	48.8	18.7	83.4	17.0	149.6	31.0
	Disc (%)>10%																																	
19HYI-9 - 20	229	0	179	407	0.44	0.1607	0.0016	8.7638	0.1352	0.3946	0.0046	2465	17	2314	14	2144	21	13.01	18.3	797	1.8	27.9	0.6	3.1	1.9	0.6	11.0	4.0	48.2	19.5	92.5	20.7	199.2	43.7
19HYI-9 - 13	251	1	195	483	0.40	0.1590	0.0014	8.4746	0.3057	0.3849	0.0123	2456	14	2283	33	2099	57	14.52	26.6	835	0.3	21.7	0.3	2.1	2.2	0.8	8.9	3.0	35.5	14.4	68.7	15.7	157.3	37.2
19HYI-9 - 15	239	1	220	431	0.51	0.1614	0.0013	8.9748	0.2582	0.4016	0.0102	2472	14	2335	26	2177	47	11.96	18.9	800	0.1	22.3	0.2	2.1	2.4	1.6	11.5	3.8	44.3	17.9	83.0	19.2	186.6	42.1
19HYI-9 - 16	171	0	237	275	0.86	0.1626	0.0016	8.9782	0.2027	0.3991	0.0071	2483	17	2336	21	2165	33	12.82	25.6	831	0.2	45.8	0.3	2.9	4.6	1.5	22.9	7.5	85.3	33.2	151.5	34.0	322.1	70.8
19HYI-9 - 18	156	0	135	354	0.38	0.1604	0.0016	6.8305	0.1085	0.3083	0.0035	2461	17	2090	14	1732	17	29.61	24.2	825	1.5	24.1	0.6	3.2	2.2	0.7	6.7	2.1	26.5	10.8	50.4	11.9	122.2	29.2
	Later-thernmal-event zircon																																	
19HYI-9 - 08	219	0	226	328	0.69	0.1565	0.0014	9.5219	0.1150	0.4412	0.0037	2418	15	2390	11	2356	16	2.57	11.1	750	0.1	20.1	0.1	0.9	2.0	0.4	9.3	3.2	38.0	14.2	63.4	13.8	127.6	26.2
19HYI-9 - 19	195	5	153	341	0.45	0.1547	0.0014	8.6588	0.0961	0.4053	0.0030	2399	16	2303	10	2193	14	8.58	18.7	799	0.2	15.7	0.1	1.1	1.4	0.3	6.0	2.2	26.1	10.5	50.4	11.7	117.5	28.2
19HYI-9 - 10	190	3	178	327	0.55	0.1533	0.0018	8.3013	0.1813	0.3928	0.0073	2384	19	2264	20	2136	34	10.40	17.1	790	0.2	17.6	0.2	1.5	1.9	1.0	9.1	2.9	34.1	13.3	62.0	14.1	142.3	32.3
19HYI-9 - 12	219	7	186	407	0.46	0.1545	0.0014	8.4498	0.1617	0.3972	0.0074	2396	16	2281	17	2156	34	10.01	19.1	801	0.4	25.3	0.3	2.3	2.3	0.8	12.5	4.6	56.1	22.7	106.7	23.7	231.3	51.6
	Trapped zircon																																	
19HYI-9 - 02	142	1	52	232	0.22	0.1842	0.0022	12.0591	0.3236	0.4717	0.0094	2690	19	2609	25	2491	41	7.41	62.8	933	0.4	12.0	0.5	3.5	2.9	0.9	10.0	3.6	41.2	16.3	75.4	18.3	185.6	43.1
19HYI-9 - 06	106	5	75	140	0.54	0.1886	0.0020	13.7869	0.2961	0.5280	0.0083	2731	17	2735	20	2733	35	-0.06	39.8	879	0.1	16.0	0.1	0.7	1.2	0.3	7.0	2.8	31.7	13.1	60.6	13.9	131.9	28.5
19HYI-9 - 07	119	0	101	154	0.66	0.1825	0.0024	13.7311	0.3679	0.5416	0.0096	2675	22	2731	25	2790	40	-4.31	14.0	771	25.6	77.3	7.4	28.4	6.3	0.9	13.0	3.7	42.5	16.1	69.4	15.4	142.8	30.9
A-1-1	Triassic quartz monzonite porphyry																																	
	Magmatic zircon																																	
A-1-1-01	23	0	319	519	0.61	0.0548	0.0021	0.2642	0.0091	0.0352	0.0004	406	85	238	7	223	2	6.21	5.0	684	0.1	41.4	0.3	3.5	6.1	3.3	28.1	8.2	85.7	31.5	141.7	30.8	292.2	62.4
A-1-1-02	10	1	88	251	0.35	0.0537	0.0021	0.2611	0.0084	0.0351	0.0003	367	95	236	7	222	2	5.56	3.7	660	0.0	18.5	0.0	0.9	2.1	1.5	13.5	4.3	47.4	18.1	84.7	19.1	184.6	40.9
A-1-1-03	20	1	270	482	0.56	0.0551	0.0018	0.2638	0.0073	0.0346	0.0003	417	79	238	6	219	2	7.74	4.2	670	0.1	35.8	0.3	4.6	9.1	5.9	42.5	11.1	113.4	39.8	172.5	35.9	329.7	69.3
A-1-1-07	11	0	110	256	0.43	0.0542	0.0019	0.2656	0.0095	0.0354	0.0004	389	78	239	8	225	2	6.11	2.8	640	0.0	24.8	0.1	1.4	2.7	1.6	14.9	4.4	49.7	18.1	82.5	18.1	175.4	38.9
A-1-1-08	13	0	169	283	0.59	0.0514	0.0023	0.2576	0.0095	0.0360	0.0004	261	106	233	8	228	3	2.08	3.6	659	0.0	39.2	0.2	3.7	5.7	3.1	23.8	6.5	73.1	26.7	118.5	25.6	242.8	52.2
A-1-1-09	13	1	140	324	0.43	0.0518	0.0016	0.2495	0.0081	0.0349	0.0004	276	69	226	7	221	2	2.36	3.2	649	0.0	31.4	0.1	1.4	3.4	2.0	18.7	5.9	63.6	24.3	109.8	23.9	226.7	48.7
A-1-1-10	21	1	284	485	0.59	0.0503	0.0015	0.2435	0.0068	0.0351	0.0003	209	69	221	6	222	2	-0.53	3.8	663	0.0	54.1	0.1	2.6	6.5	3.1	30.2	9.3	100.2	36.8	161.0	33.2	305.3	63.3
	Trapped zircon																																	
A-1-1-05	26	5	56	524	0.11	0.0540	0.0027	0.3187	0.0180	0.0406	0.0010	372	115	281	14	257	6	8.68	5.1	685	0.0	120.9	0.2	3.7	8.3	4.4	46.0	13.0	141.5	50.2	211.4	42.6	374.5	75.8
A-1-1-04	104	1	28	218	0.13	0.1488	0.0026	8.4459	0.2507	0.4055	0.0068	2332	30	2280	27	2194	31	3.77	8.4	726	0.0	5.0	0.0	1.0	2.1	0.4	11.6	3.3	34.3	11.3	47.5	10.0	97.6	22.1
A-1-1-06	18	1	75	140	0.53	0.1033	0.0046	3.4518	0.3715	0.1854	0.0161	1684	83	1516	85	1096	88	27.70	4.8	681	0.1	19.5	0.1	1.3	3.1	1.2	14.0	3.8	38.2	13.1	55.0	11.3	104.9	21.4
B-1-1G	Triassic quartz monzonite porphyry																																	
	Magmatic zircon																																	
B-1-1G-01	23	1	242	553	0.44	0.0516	0.0015	0.2592	0.0074	0.0363	0.0004	333	67	234	6	230	2	1.77	3.1	648	0.0	42.5	0.1	2.0	5.4	3.2	31.4	10.5	123.6	46.9	213.1	44.9	412.7	87.0
B-1-1G-02	20	1	558	353	1.58	0.0530	0.0022	0.2642	0.0112	0.0358	0.0004	332	94	238	9	227	2	4.70	5.9	697	2.3	61.6	1.0	8.9	9.9	4.5	37.3	9.1	87.5	29.1	123.0	25.4	228.8	50.5
B-1-1G-03	25	0	209	610	0.34	0.0504	0.0014	0.2526	0.0067	0.0362	0.0003	213	61	229	5	229	2	-0.22	2.3	627	0.0	26.3	0.0	1.0	3.7	2.6	25.3	8.7	101.1	40.3	189.3	40.6	377.2	81.1
B-1-1G-04	10	1	97	228	0.42	0.0498	0.0020	0.2470	0.0092	0.0361	0.0004	187	88	224	8	228	2	-1.94	1.6	601	0.0	22.1	0.0	0.9	2.4	1.3	13.0	4.0	44.5	16.4	76.3	16.9	164.6	35.7
B-1-1G-07	14	0	191	322	0.59	0.0493	0.0018	0.2446	0.0085	0.0361	0.0004	161	90	222	7	228	3	-2.80	3.6	657	0.0	39.6	0.1	2.2	4.5	2.5	21.6	6.3	68.3	26.0	117.4	25.8	243.9	53.7
B-1-1G-08	27	1	395	631	0.63	0.0515	0.0014	0.2533	0.0069	0.0355	0.0003	265	63	229	6	225	2	1.93	2.7	637	0.0	51.9	0.1	1.8	4.5	2.5	26.2	7.8	80.5	28.6	125.6	26.8	243.1	51.6
B-1-1G-09	26	1	435	575	0.76	0.0507	0.0013	0.2483	0.0063	0.0354	0.0003	228	61	225	5	224	2	0.40	3.9	664	0.2	58.8	0.2	2.9	6.9	3.4	30.0	8.2	82.7	28.3	121.3	24.6	221.7	46.5
B-1-1G-10	10	1	105	224	0.47	0.0490	0.0025	0.2431	0.0104	0.0360	0.0005	146	114	221	9	228	3	-3.32	2.9	643	0.0	25.6	0.1	1.4	2.9	1.7	14.8	4.3	47.6	17.8	81.1	17.9	167.8	36.9
	Trapped zircon																																	
B-1-1G-05	14	1	28	34	0.83	0.1188	0.0034	5.4345	0.1837	0.3291	0.0062	1939	50	1890	29	1834	30	2.99	9.5	737	0.0	6.4	0.0	0.4	1.2	0.2	5.3	1.5	15.6	5.2	21.3	4.2	37.0	7.8
B-1-1G-06	13	1	20	36	0.56	0.1122	0.0032	4.5500	0.1588	0.2938	0.0070	1835	53	1740	29	1660	35	4.59	7.3	714	0.0	5.8	0.0	0.6	0.9	0.2	5.2	1.6	16.7	5.8	24.5	4.9	45.7	9.5
A-2-1	Triassic lamprophyre																																	
	Magmatic zircon																																	
A-2-1-01	30	1	823	630	1.31	0.0484	0.0015	0.2366	0.0071	0.0354	0.0003	117	66	216	6	224	2	-3.93	28.1	841	15.4	79.8	7.8	39.2	13.5	6.4	28.9	7.3	75.0	26.9	115.7	24.9	237.6	52.3
A-2-1-03	35	0	657	666	0.99	0.0540	0.0013	0.2928	0.0067	0.0392	0.0003	372	58	261	5	248	2	4.92	6.1	700	18.8	62.4	4.6	22.3	10.8	3.1	31.8	8.9	92.3	32.9	142.1	30.1	280.8	60.4
A-2-1-07	30	0	512	610	0.84	0.0547	0.0015	0.2866	0.0079	0.0379	0.0003	398	58	256	6	240	2	6.24	6.5	705	0.3	23.4	0.2	2.7	3.6	1.4	15.2	4.9	56.6	22.1	100.8	22.9	221.7	49.6
A-2-1-05	41	1	728	807	0.90	0.0539	0.0014	0.2880	0.0073	0.0386	0.0003	369	62	257	6	244	2	5.10	7.7	719	0.7	28.8	0.2	3.0	4.0	1.6	20.2	6.2	74.5	28.9	130.8	28.4	277.9	60.2
	Trapped zircon																																	
A-2-1-02	62	0	74	396	0.19	0.0731	0.0012	1.4481	0.0272	0.1430	0.0015	1017	33	909	11	862	8	5.22	2.3	627	0.0	1.5	0.0	0.1	0.2	0.1	1.6	0.7	9.3	4.2	22.6	5.7	64.5	18.2
A-2-1-04	42	1	409	352	1.16	0.0646	0.0025	0.7898	0.0189	0.0880	0.0007	761	80	591	11	544	4	8.05	339.0	1187	81.8	209.6	23.9	109.3	30.5	1.9	45.1	9.6	86.2	30.0	140.2	34.1	348.5	81.0
A-2-1-06	62	3	203	186	1.09	0.0950	0.0022	3.0331	0.0793	0.2299	0.0030	1528	43	1416	20	1334	15	5.79	160.5	1062	0.7	76.9	1.3	10.9	11.4	3.9	44.0	13.4	149.2	53.6	236.6	48.6	451.5	92.8
A-2-1-08	184	1	654	1468	0.45	0.0691	0.0016	1.0017	0.0198	0.1049	0.0014	902	47	705	10	643	8	8.77	7.0	711	0.1	41.1	0.3	4.0	5.5	1.3	28.6	10.0	126.7	48.2	219.2	47.6	452.2	95.5
A-2-1-09	167	0	404	649	0.62	0.0855	0.0014	2.4659	0.0515	0.2079	0.0027	1326	36	1262	15	1218	14	3.52	9.0	732	0.0	13.6	0.3	4.3	8.3	0.3	45.8	15.6	180.8	67.9	290.1	57.3	491.6	96.2
A-2-1-10	31	0	139	193	0.72	0.0691	0.0022	1.1873	0.0269	0.1240	0.0009	903	67	795	13	754	5	5.14	3.7	661	0.0	19.5	0.1	1.3	2.6	0.9	14.7	4.8	57.9	22.9	106.6	24.1	235.3	53.7
B-2-1G	Triassic lamprophyre																																	
	Magmatic zircon																																	
B-2-1G-12	33	0	447	844	0.53	0.0548	0.0020	0.2627	0.0074	0.0345	0.0003	406	81	237	6	219	2	7.55	87.9	976	20.8	104.3	18.1	103.5	59.8	4.0	139.2	42.7	461.4	160.2	685.5	137.3	1203.3	233.0
B-2-1G-15	9	0	13	213	0.06	0.0547	0.0026	0.2893	0.0121	0.0380	0.0004	467	101	258	10	240	3	6.79	11.6	754	0.2	5.1	0.1	0.8	0.5	0.3	2.9	1.0	13.1	6.2	34.6	8.8	102.6	26.5
	Trapped zircon																																	
B-2-1G-13	18	1	51	406	0.13	0.0532	0.0015	0.3128	0.0088	0.0425	0.0003	339	67	276	7	268	2	2.85	11.0	749	0.0	0.8	0.1	1.4	4.6	0.1	36.1	18.8	276.5	116.6	567.1	121.4	1080.9	213.9
B-2-1G-06	22	1	256	413	0.62	0.0545	0.0016	0.3222	0.0092	0.0428	0.0004	394	65	284	7	270	2	4.83	12.0	757	0.0	3.2	0.2	3.4	8.1	0.2	54.3	20.1	250.1	95.8	420.8	84.2	711.0	139.9
B-2-1G-09	20	0	174	376	0.46	0.0546	0.0017	0.3453	0.0108	0.0457	0.0004	394	69	301	8	288	3	4.36	23.8	823	0.1	2.5	0.2	2.9	7.4	0.1	55.8	21.6	285.0	111.4	509.0	102.9	890.0	176.3
B-2-1G-14	19	1	119	363	0.33	0.0540	0.0015	0.3480	0.0091	0.0466	0.0004	372	61	303	7	293	2	3.21	8.1	723	0.1	9.9	0.1	1.9	5.3	0.6	43.3	19.8	276.0	116.2	554.0	116.7	1039.5	205.7
B-2-1G-03	24	0	249	380	0.65	0.0554	0.0016	0.3867	0.0114	0.0504	0.0005	428	63	332	8	317	3	4.49	5.4	689	0.0	8.7	0.1	2.2	5.7	0.9	35.8	14.1	178.3	71.3	333.8	69.8	641.1	134.5
B-2-1G-01	30	0	108	537	0.20	0.0531	0.0013	0.3765	0.0110	0.0509	0.0007	345	56	324	8	320	4	1.44	9.6	738	1.3	7.1	0.9	5.7	6.3	0.4	31.3	12.6	158.2	61.4	286.8	61.0	555.3	116.7
B-2-1G-05	21	1	161	349	0.46	0.0555	0.0016	0.3957	0.0111	0.0517	0.0006	435	63	339	8	325	3	3.98	31.1	851	0.9	12.5	1.5	9.7	9.3	0.8	38.3	16.2	212.1	85.9	397.7	84.8	747.6	150.6
B-2-1G-11	26	0	280	382	0.73	0.0550	0.0015	0.4081	0.0110	0.0537	0.0004	413	63	348	8	337	3	2.89	23.0	820	0.0	36.8	0.1	2.5	6.5	1.8	38.8	13.4	159.8	63.0	279.4	56.8	501.5	103.9
B-2-1G-04	69	1	85	731	0.12	0.0631	0.0019	0.7707	0.0180	0.0876	0.0010	722	60	580	10	541	6	6.72	10.9	748	0.9	7.1	1.1	7.3	10.3	4.9	40.1	15.7	197.7	77.1	365.1	79.5	724.9	145.4
B-2-1G-08	36	0	36	60	0.60	0.1723	0.0030	11.1011	0.1944	0.4657	0.0036	2580	29	2532	16	2465	16	2.65	6.3	701	0.0	1.3	0.0	0.2	0.6	0.3	4.9	1.5	16.7	5.7	23.3	4.3	37.8	7.4
B-2-1G-07	50	0	134	317	0.42	0.0848	0.0031	1.5079	0.0290	0.1279	0.0010	1311	72	934	12	776	6	16.91	15.2	779	0.5	10.0	0.3	2.4	4.3	0.3	27.0	10.6	138.6	56.7	260.5	54.6	487.2	98.5
	Outliers																																	
B-2-1G-02	41	2	1374	3408	0.40	0.0508	0.0013	0.0736	0.0026	0.0105	0.0003	232	66	72	2	67	2	6.51	5.8	696	0.7	20.0	0.6	4.0	5.5	0.5	34.7	14.5	192.7	80.2	389.6	87.1	822.5	181.5
B-2-1G-10	2	1	71	56	1.27	0.0535	0.0046	0.1568	0.0110	0.0217	0.0005	350	194	148	10	138	3	6.57	27.2	837	0.0	56.1	0.3	3.9	6.0	1.0	24.5	7.3	80.2	27.6	117.3	23.8	211.5	43.9
YJT-3-1G	Early Cretaceous diabase																																	
	Magmatic zircon																																	
YJT-3-1G-01	7	1	284	284	1.00	0.0524	0.0031	0.1444	0.0085	0.0198	0.0003	302	132	137	8	127	2	7.60	7.4	715	4.1	61.5	0.7	5.4	6.8	1.6	30.3	9.4	105.3	40.0	184.7	41.4	404.4	89.3
YJT-3-1G-02	5	0	128	181	0.71	0.0548	0.0036	0.1559	0.0082	0.0212	0.0004	467	146	147	7	135	2	8.18	7.2	713	0.6	49.5	0.8	6.4	5.7	1.8	18.9	6.3	74.2	27.7	126.5	27.3	257.9	52.7
YJT-3-1G-03	4	0	132	141	0.93	0.0512	0.0034	0.1387	0.0079	0.0201	0.0003	250	147	132	7	128	2	2.79	8.1	723	1.4	65.8	0.5	4.1	4.9	1.0	22.4	7.6	91.3	34.6	160.2	34.9	330.8	69.8
YJT-3-1G-05	2	0	78	74	1.06	0.0541	0.0051	0.1473	0.0113	0.0206	0.0004	376	215	140	10	131	3	5.91	10.4	744	81.7	172.4	10.4	34.6	6.7	1.2	15.7	4.8	54.4	20.2	89.7	18.6	171.7	35.6
YJT-3-1G-06	3	0	88	109	0.81	0.0468	0.0035	0.1271	0.0079	0.0202	0.0003	39	170	121	7	129	2	-6.09	6.9	709	0.0	47.8	0.1	1.4	2.9	0.7	14.1	4.9	57.8	23.2	106.6	23.8	229.0	49.2
YJT-3-1G-08	3	1	105	121	0.87	0.0511	0.0032	0.1391	0.0078	0.0200	0.0004	256	143	132	7	128	2	3.49	7.9	721	17.4	91.5	4.5	20.3	7.5	1.2	22.2	7.3	84.2	32.0	144.9	31.7	301.1	62.3
YJT-3-1G-09	4	0	127	142	0.89	0.0501	0.0034	0.1348	0.0086	0.0197	0.0004	211	156	128	8	125	2	2.25	9.4	735	0.2	61.2	0.2	2.4	4.1	0.9	21.5	7.1	87.1	34.2	156.3	34.9	330.2	68.8
YJT-3-1G-10	3	1	108	104	1.04	0.0484	0.0037	0.1294	0.0083	0.0197	0.0003	117	170	124	7	126	2	-1.70	6.6	705	0.0	50.7	0.2	2.6	5.6	1.4	27.8	8.8	102.5	37.4	167.2	34.8	323.6	65.8
YJT-3-1G-11	2	1	80	93	0.86	0.0495	0.0037	0.1347	0.0080	0.0202	0.0004	169	176	128	7	129	3	-0.59	6.4	703	0.0	51.4	0.1	1.6	3.0	0.6	15.0	4.9	57.0	21.7	98.6	21.6	199.6	42.2
YJT-3-1G-12	4	1	123	139	0.88	0.0500	0.0035	0.1354	0.0087	0.0200	0.0003	195	165	129	8	127	2	1.18	24.5	826	0.6	60.0	0.3	3.1	4.3	1.0	20.9	7.1	85.1	32.8	153.8	33.6	322.7	67.6
YJT-3-1G-13	5	0	189	188	1.01	0.0542	0.0029	0.1582	0.0082	0.0213	0.0003	389	119	149	7	136	2	8.91	198.0	1095	7.0	86.3	1.9	8.7	5.0	1.1	20.5	6.9	79.7	30.3	141.9	31.3	292.1	61.1
YJT-3-1G-14	4	1	164	153	1.07	0.0482	0.0030	0.1283	0.0068	0.0195	0.0003	109	141	123	6	125	2	-1.77	9.9	740	2.2	75.0	0.9	6.2	6.7	2.0	29.7	9.9	117.1	44.1	204.9	44.0	409.9	86.4
YJT-3-1G-15	7	0	231	276	0.83	0.0491	0.0028	0.1387	0.0069	0.0206	0.0003	154	135	132	6	132	2	0.12	8.1	722	2.2	66.8	0.8	5.7	5.4	1.0	24.5	8.5	104.1	39.3	182.3	39.1	362.9	74.0
YJT-3-1G-16	5	0	268	180	1.49	0.0510	0.0033	0.1410	0.0068	0.0204	0.0003	239	150	134	6	130	2	2.62	13.3	766	153.4	363.4	39.9	170.4	33.4	5.4	54.0	12.7	127.1	44.1	185.8	36.8	322.5	65.5
YJT-3-1G-18	6	0	320	179	1.79	0.0506	0.0027	0.1456	0.0069	0.0212	0.0003	220	122	138	6	135	2	2.22	9.5	736	16.3	122.4	4.3	20.2	12.0	2.5	41.9	13.0	140.9	48.7	205.2	41.5	369.8	73.5
YJT-3-1G-19	3	0	96	108	0.89	0.0476	0.0033	0.1337	0.0080	0.0208	0.0004	80	156	127	7	133	2	-4.04	7.3	713	1.5	48.1	0.3	3.3	5.0	0.9	22.3	7.3	83.5	30.6	138.1	29.7	280.4	58.0
YJT-3-1G-20	10	0	276	389	0.71	0.0500	0.0022	0.1420	0.0064	0.0206	0.0002	195	104	135	6	131	1	2.58	2.9	642	10.9	50.5	1.1	3.7	2.1	0.5	8.6	3.0	35.9	15.4	76.2	18.6	200.4	51.8
YJT-3-1G-07	4	1	152	140	1.09	0.0670	0.0049	0.1717	0.0104	0.0192	0.0004	839	153	161	9	123	2	23.67	9.2	734	0.1	43.4	0.1	2.2	3.7	1.0	17.6	5.9	66.5	24.5	109.1	23.1	211.0	43.4
YJT-3-1G-17	10	2	642	310	2.07	0.0734	0.0039	0.1976	0.0112	0.0193	0.0002	1025	107	183	10	123	2	32.72	36.6	869	1.1	224.2	1.3	17.1	25.7	5.4	102.3	29.7	313.6	104.3	425.1	82.9	713.5	136.1
	Disc (%)>10%																																	
YJT-3-1G-04	5	2	106	98	1.08	0.2317	0.0141	0.8145	0.0589	0.0244	0.0005	3064	98	605	33	156	3	74.29	49.6	904	94.9	235.1	20.5	74.1	14.9	3.1	28.9	8.2	91.0	32.7	145.6	30.9	282.6	58.9

Notes: Degree of discordance = 100 × (1 − ($^{206}Pb/^{238}U$ age/$^{207}Pb/^{206}Pb$ age)), $\lambda^{238}U = 0.0155125 \times 10^{-9}\ yr^{-1}$, $\lambda^{235}U = 0.98485 \times 10^{-9}\ yr^{-1}$, $\lambda^{232}Th = 0.049475 \times 10^{-9}\ yr^{-1}$.
The Ti-in-zircon thermometer calibrated by Ferry and Watson (2007) was used to estimate the magmatic or metamorphic temperatures in studied sample.
Ferry, J.M., Watson, E.B., 2007. New thermodynamic models and revised calibrations for the Ti–in–zircon and Zr–in–rutile thermometers. Contributions to Mineralogy and Petrology, 154, 429–437.

Paleoproterozoic (1835 ± 53 Ma, 1939 ± 50 Ma, and 2332 ± 30 Ma) to the Paleozoic (257 ± 6 Ma) (Table 1).

4.1.3. Late Triassic lamprophyre

Zircon grains obtained from Sample A-2–1 are generally khaki to deep yellow, transparent to translucent, and mostly euhedral prismatic crystals, with long axes of 60–120 μm. In CL images, most grains appear dark with either weak internal oscillatory zoning or misty internal structures (Fig. 3d). These features, combined with high Th and U contents (512–823 ppm and 610–807 ppm, respectively), and Th/U ratios (0.84–1.31) (Table 1), indicate a typical mafic magmatic origin for these zircons (Baines et al., 2009; Hoskin, 2001; Koglin et al., 2009; Pupin, 1980). Four zircon analyses yield an upper intercept age of 231 ± 47 Ma (MSWD = 1.2), consistent with the $^{206}Pb/^{238}U$ weighted mean age of 239 ± 17 Ma (MSWD = 4.4) obtained from concordant or nearly concordant zircons. We interpret the weighted mean $^{206}Pb/^{238}U$ age of approximately 230 Ma as the emplacement age (Fig. 4d). The remaining grains are trapped zircons that display relatively complex internal structures, such as core–rim structure, with Mesoproterozoic to Neoproterozoic ages (1528 ± 43 Ma to 544 ± 4 Ma) and low degrees of discordance (Fig. 4d; Table 1).

Zircon grains obtained from Sample B-2-1G are generally pale yellow, transparent, and mostly euhedral prismatic crystals, with long axes of 50–80 μm. In CL images, grain #12 displays internal oscillatory zoning (Fig. 3e) and exhibits high Th and U contents (447 ppm and 844 ppm, respectively), and a Th/U ratio of 0.53 (Table 1), indicating a magmatic origin (Baines et al., 2009; Hoskin, 2000; Koglin et al., 2009; Pupin, 1980). We interpret the concordant $^{206}Pb/^{238}U$ age of approximately 220 Ma as the emplacement age (Fig. 4e). This age is identical to that of the quartz monzonite porphyry, indicating their contemporaneous emplacement during the Late Triassic. The majority of domains are trapped zircons with relatively complex internal structures, yielding ages ranging from the Archean ($^{207}Pb/^{206}Pb$ age of 2580 ± 29 Ma) to the Paleozoic ($^{206}Pb/^{238}U$ age of 268 ± 2 Ma). Outliers include a magmatic $^{206}Pb/^{238}U$ age of 138 ± 3 Ma, which corresponds to the Early Cretaceous tectono-thermal event, as evidenced by the $^{206}Pb/^{238}U$ age (Table 1) and *in-situ* Hf isotopic values (Table 2). The Late Triassic magmatic event in northwestern Beijing is revealed not only by the quartz monzonite porphyry and Triassic lamprophyre within the Mesoproterozoic cover, as discussed in this study, but also by monzonite porphyry sills from other localities in northwestern Beijing (Ji et al., 2017). Furthermore, aplite dykes, with a weighted mean $^{206}Pb/^{238}U$ age of 206 ± 4 Ma, cross-cut the aforementioned sills (Ji et al., 2017) (Fig. 1c), indicating that the emplacement age of mafic to intermediate sills predates 206 Ma.

4.1.4. Early Cretaceous diabase

Zircon grains obtained from the Early Cretaceous diabase sample are generally pale yellow, transparent, and mostly subhedral columnar, with long axes of 100–200 μm. In CL images, most grains exhibit strong oscillatory zoning (Fig. 3f). These features, together with their varied Th and U contents (78–642 ppm and 74–389 ppm, respectively), and high Th/U ratios (0.71–2.07) (Table 1), indicate a typical magmatic origin for these zircons (Baines et al., 2009; Hoskin, 2000; Koglin et al., 2009; Pupin, 1980). Twenty zircon analyses from Sample YJT-3-1G define an upper intercept age of 128 ± 3 Ma (MSWD = 20.0), consistent with the $^{206}Pb/^{238}U$ weighted mean age of 129 ± 2 Ma (MSWD = 15.0) obtained from all nineteen concordant zircons (Fig. 4f). We interpret the weighted mean $^{206}Pb/^{238}U$ age of approximately 130 Ma as the emplacement age of the Early Cretaceous diabase dyke.

Table 2
Zircon Hf isotopic data.

No.	t(Ma)	$^{176}Yb/^{177}Hf$	$^{176}Lu/^{177}Hf$	$^{176}Hf/^{177}Hf$	±2σ	εHf(t)	±2σ	T_{Hf}(Ma)	T_{Hf2}(Ma)	$f_{Lu/Hf}$
A-1-1	Triassic quartz monzonite porphyry									
	Magmatic zircon									
A-1-1-01	223	0.030512	0.000997	0.282220	0.000009	−14.8	0.3	1456	3019	−0.97
A-1-1-02	222	0.034746	0.001161	0.282213	0.000009	−15.1	0.3	1471	3042	−0.97
A-1-1-03	219	0.032245	0.001085	0.282235	0.000011	−14.3	0.4	1438	2977	−0.97
A-1-1-07	225	0.039515	0.001246	0.282233	0.000009	−14.3	0.3	1446	2977	−0.96
A-1-1-08	228	0.033885	0.001061	0.282234	0.000009	−14.2	0.3	1438	2969	−0.97
A-1-1-09	221	0.026815	0.000888	0.282229	0.000009	−14.5	0.3	1439	2991	−0.97
A-1-1-10	222	0.033656	0.001101	0.282231	0.000011	−14.4	0.4	1444	2985	−0.97
B-1-1G	Triassic quartz monzonite porphyry									
	Magmatic zircon									
B-1-1G-01	230	0.029245	0.000914	0.282243	0.000010	−13.8	0.4	1420	2935	−0.97
B-1-1G-02	227	0.032067	0.000993	0.282250	0.000011	−13.6	0.4	1413	2917	−0.97
B-1-1G-03	229	0.044660	0.001410	0.282211	0.000010	−15.0	0.4	1483	3043	−0.96
B-1-1G-04	228	0.032614	0.001039	0.282262	0.000009	−13.2	0.3	1398	2878	−0.97
B-1-1G-07	228	0.026855	0.000854	0.282243	0.000010	−13.8	0.4	1417	2936	−0.97
B-1-1G-08	225	0.024242	0.000779	0.282267	0.000014	−13.0	0.5	1381	2864	−0.98
B-1-1G-09	224	0.025135	0.000817	0.282230	0.000011	−14.4	0.4	1434	2982	−0.98
B-1-1G-10	228	0.028777	0.000942	0.282241	0.000010	−13.9	0.4	1423	2943	−0.97
	Trapped zircon									
B-1-1G-05	1939	0.005480	0.000174	0.281373	0.000010	−6.4	0.4	2567	3395	−0.99
B-1-1G-06	1835	0.005324	0.000168	0.281367	0.000008	−9.0	0.3	2575	3552	−0.99
A-2-1	Triassic lamprophyre									
	Magmatic zircon									
A-2-1-01	224	0.019354	0.000712	0.282817	0.000010	6.4	0.3	611	1109	−0.98
A-2-1-03	248	0.031619	0.001172	0.282807	0.000017	6.5	0.6	633	1118	−0.96
A-2-1-05	244	0.023643	0.000893	0.282877	0.000015	8.9	0.5	531	896	−0.97
A-2-1-07	240	0.019848	0.000734	0.282820	0.000012	6.9	0.4	608	1081	−0.98
B-2-1G	Triassic lamprophyre									
	Magmatic zircon									
B-2-1G-12	219	0.112238	0.003721	0.282591	0.000017	−2.1	0.6	1008	1879	−0.89
B-2-1G-15	240	0.010139	0.000446	0.281890	0.000021	−26.0	0.8	1886	4027	−0.99
	Trapped zircon									
B-2-1G-13	268	0.087385	0.002802	0.282635	0.000015	0.6	0.5	918	1670	−0.92
B-2-1G-06	270	0.095595	0.003077	0.282631	0.000020	0.4	0.7	931	1685	−0.91
B-2-1G-09	288	0.099047	0.002944	0.282663	0.000013	1.9	0.5	879	1559	−0.91
B-2-1G-14	293	0.117089	0.003823	0.282575	0.000018	−1.3	0.6	1036	1850	−0.88
B-2-1G-03	317	0.054152	0.001834	0.282573	0.000009	−0.5	0.3	983	1794	−0.94
B-2-1G-01	320	0.101156	0.003071	0.282635	0.000011	1.6	0.4	924	1614	−0.91
B-2-1G-05	325	0.059538	0.001857	0.282455	0.000009	−4.5	0.3	1152	2158	−0.94
B-2-1G-11	337	0.065684	0.002174	0.282504	0.000017	−2.5	0.6	1091	1994	−0.93
B-2-1G-04	541	0.083718	0.002469	0.282549	0.000009	3.2	0.3	1035	1617	−0.93
B-2-1G-08	2580	0.009221	0.000318	0.281398	0.000014	8.9	0.5	2543	2495	−0.99
	Outliers									
B-2-1G-10	138	0.021751	0.000711	0.282346	0.000011	−12.1	0.4	1269	2723	−0.98

4.2. Zircon Hf isotopes

In-*situ* Hf isotopic analyses of zircons from five samples are listed in Table 2 and shown in Fig. 5a. The dashed circles in Fig. 3 represent Hf isotope analysis sites for the representative individual zircon domains. The Late Triassic quartz monzonite porphyries and Late Triassic lamprophyres display distinct zircon Hf isotopic compositions. Zircons from the Late Triassic quartz monzonite porphyries yield $^{176}Hf/^{177}Hf$ ratios ranging from 0.28221 to 0.28227, with $\varepsilon_{Hf}(t)$ values between −15.1 and −13.0 (Fig. 5a). The depleted mantle model ages (T_{Hf}) range from 1.4 to 1.5 Ga, while the crustal model ages (T_{Hf2}) range from 2.9 to 3.0 Ga (Table 2). In contrast, zircons from the Late Triassic lamprophyre (Sample A-2–1) show homogeneous $^{176}Hf/^{177}Hf$ ratios (0.28281 to 0.28287), with $\varepsilon_{Hf}(t)$ values ranging from 6.4 to 8.9 (Fig. 5a). The depleted mantle model ages (T_{Hf}) range with 0.5 to 0.6 Ga, and the crustal model ages (T_{Hf2}) range from 0.9 to 1.1 Ga (Table 2). Meanwhile, zircons from Sample B-2-1G exhibit heterogeneous $^{176}Hf/^{177}Hf$ ratios (0.28140 to 0.28266) with $\varepsilon_{Hf}(t)$ values ranging from −4.5 to 3.2 (Fig. 5a). Their depleted mantle model ages (T_{Hf}) range from 0.9 to 1.2 Ga, and the crustal model ages (T_{Hf2}) range from 1.5 to 2.2 Ga (Table 2). The Early Cretaceous zircons exhibit homogeneous $^{176}Hf/^{177}Hf$ ratios (0.28224 to 0.28242) with $\varepsilon_{Hf}(t)$ values ranging from −16.1 to −9.5. Their depleted mantle model ages (T_{Hf}) range from 1.2 Ga to 1.4 Ga, while the crustal model ages (T_{Hf2}) range from 2.5 to 3.1 Ga. This group includes magmatic zircons from the Early Cretaceous diabase as well as outliers or zircons formed or recrystallized during later thermal events in the Late Triassic lamprophyre.

4.3. Major and trace element data

The geochemical compositions of the Late Triassic lamprophyres and quartz monzonite porphyries, combined with previously published data on these mafic to intermediate dykes in northwestern Beijing, are listed in Table 3 and compared with the present data in the following figures (Figs. 6–11). The lamprophyres in northwestern Beijing are silica-undersaturated with relatively low silica contents, ranging from 46.2 % in the most primitive sample to 51.2 % in the most evolved sample (Fig. 6a and b). The lamprophyre samples also show a wide range of Al_2O_3 (12.45–16.32 wt%) and MgO (3.41–9.12 wt%) concentrations, with high $Mg^{\#}$ (molar $Mg/(Mg + Fe^{2+})$ = 40–71; averaging 58) (Supplementary Figs. 1 and 2; Table 3). They exhibit relatively high concentrations of alkali metals ($Na_2O + K_2O$ = 5.2–7.5 wt%) and are generally classified as foid gabbro, monzogabbro, and monzodiorite of alkaline affinity in the total-alkali versus silica (TAS) diagram (Irvine and Baragar, 1971; Middlemost, 1994) (Fig. 6a). This classification is distinct from Carboniferous to Permian mafic rocks, which are characterized by low K_2O and total alkali contents (Zhang et al., 2009a–c). The lamprophyres also display shoshonitic characteristics, with elevated K_2O/Na_2O ratios (0.6–1.5; Le Maitre, 2002) (Fig. 6c). According to the classification scheme of Rock (1987) in the K_2O vs. SiO_2 diagram (Fig. 6b), they belong to the calc-alkali lamprophyre field. Most samples are transitional between Groups I (anorogenic lamproites) and III (orogenic ultrapotassic series) in the ultrapotassic discrimination diagram, with CaO contents of 5.4–8.7 wt% (Foley et al., 1987; Miller et al., 1999) (Fig. 6d). The lamprophyres are also characterized by relatively high total FeO (7.28–10.24 wt%), TiO_2 (0.96–1.87 wt%), MnO (0.08–0.13 wt%), CaO (5.43–8.69 wt%), Cr (15.70–86.72 ppm) and Ni (23.30–44.00 ppm) abundances (Supplementary Figs. 1 and 2; Table 3). In comparison, quartz monzonite porphyries have higher and more restricted SiO_2 contents (61.14–64.59 wt%) and relatively low MgO concentrations (1.28–2.07 wt%), with high $Mg^{\#}$ (44–58; averaging 51). Quartz monzonite porphyries plot near the boundary between the alkaline and calc-alkaline series (Fig. 6a) and exhibit shoshonitic characteristics (K_2O/Na_2O ratios of 0.8–2.6; Fig. 6b, c). They are also enriched in total FeO (2.81–3.25 wt%), TiO_2 (0.36–0.41 wt%), MnO (0.05–0.06 wt%), CaO (1.68–3.22 wt%), Cr (23.20–26.40 ppm), and Ni (21.20–23.40 ppm) (Table 3).

The studied samples in this contribution exhibit uniform chondrite-normalized REE patterns. Both the lamprophyres and quartz monzonite porphyries are enriched in light rare earth elements (LREEs), with $(La/Yb)_N$ ratios (subscript N denotes chondrite normalization) of 25.8–39.2 (averaging 33.7) and 56.0–61.0 (averaging 57.5), respectively (Fig. 7a). These values suggest the possibility that these mafic to intermediate sills are spatially and temporally cognate. Both groups exhibit slightly negative to positive Eu anomalies (0.9–1.1; averaging 1.0) and negative Ce anomalies (0.8–1.0; averaging 0.9) in chondrite-normalized REE patterns. Additionally, they display negative P and Ti anomalies as shown in the primitive mantle-normalized spider diagrams (Sun and McDonough, 1989). Most samples are enriched in large ion lithophile elements (LILEs), such as Rb, Sr, and Ba, as well as Zr and Hf, but are depleted in Nb and Ta (Fig. 7b).

4.4. Whole-rock Nd and Hf isotopes

The whole-rock Nd–Hf isotope compositions of lamprophyres and quartz monzonite porphyries are listed in Table 4. To discuss the

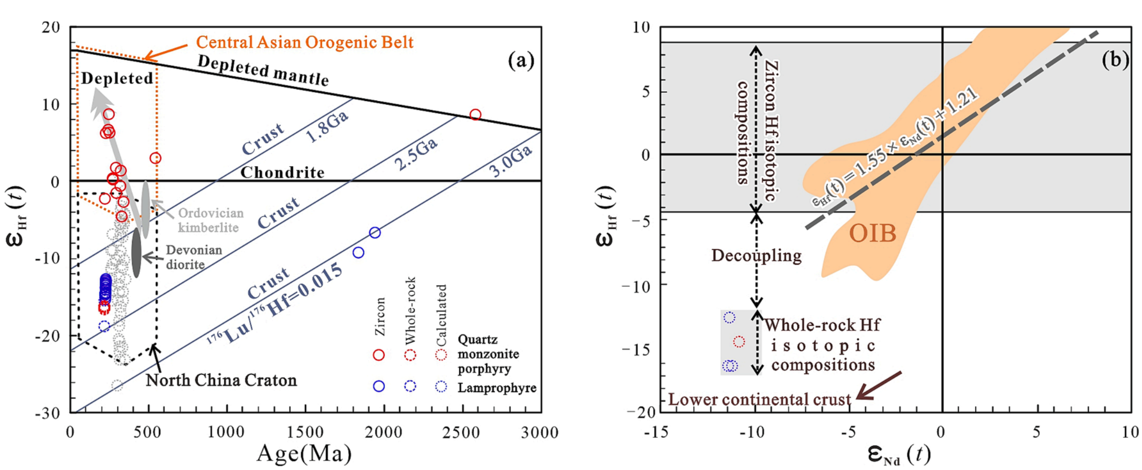

Fig. 5. (a) $\varepsilon_{Hf}(t)$ versus U–Pb age of zircons and (b) $\varepsilon_{Hf}(t)$ versus $\varepsilon_{Nd}(t)$ (Yang et al., 2007d) of Late Triassic lamprophyre and quartz monzonite porphyry sills in northwestern Beijing, northern NCC. Hf isotopic compositions of Late Triassic igneous rocks, the Middle Devonian alkaline complex and ultramafic–mafic rocks, and Late Carboniferous–Early Permian hornblende gabbros are from Zhang et al. (2007, 2009a–c, 2012), Tian et al. (2007), Wang et al. (2021) and references therein. $\Delta\varepsilon_{Hf}(t)$ is defined as $\varepsilon_{Hf}(t) = [1.55 \times \varepsilon_{Nd}(t) + 1.21]$ such that a sample with positive $\Delta\varepsilon_{Hf}(t)$ lies above and a sample with negative $\Delta\varepsilon_{Hf}(t)$ lies below the mantle array of Vervoort et al. (2011).

Table 3
Chemical data.

Sample no.	A-2-1	B-2-1G	B-3-1G	19HY1-1	BJ13-7*	BJ15-8*	BJ15-9*	BJ15-10*	BJ15-11*	A-1-1	B-1-1G	BJ13-5*	BJ13-6*
Rock type	Lamprophyre									Monzonite porphyry			
wt.%													
SiO_2	51.61	51.73	50.52	51.63	50.73	46.24	46.57	48.01	49.90	61.79	64.58	61.14	64.59
TiO_2	1.82	1.80	1.57	1.87	0.96	0.96	0.96	0.98	0.97	0.41	0.41	0.37	0.36
Al_2O_3	16.32	16.32	14.80	15.95	13.65	12.45	12.68	13.66	14.33	16.07	16.25	19.29	13.43
Fetot	9.55	9.46	8.44	10.24	7.45	7.47	7.54	7.28	7.34	3.25	3.17	2.91	2.81
MnO	0.11	0.11	0.08	0.13	0.09	0.10	0.11	0.11	0.09	0.05	0.05	0.05	0.05
MgO	3.84	3.80	3.98	3.41	7.17	9.03	9.12	8.58	8.00	1.65	1.28	2.07	1.41
CaO	5.71	5.85	5.43	8.69	5.53	7.11	7.37	6.69	5.84	3.09	1.68	2.45	3.22
Na_2O	4.37	4.73	4.07	3.05	3.79	2.79	2.88	3.07	3.03	4.20	4.38	4.05	2.13
K_2O	2.66	2.79	2.75	2.10	3.62	4.31	3.86	3.70	2.82	4.40	4.61	3.11	5.63
P_2O_5	0.90	0.88	0.77	1.04	0.57	0.49	0.48	0.57	0.60	0.23	0.27	0.19	0.20
LOI	2.51	2.05	6.72	1.57	6.13	8.63	8.05	6.89	6.68	4.01	2.69	4.12	5.85
Total	99.39	99.52	99.13	99.68	99.69	99.59	99.62	99.53	99.59	99.15	99.36	99.76	99.68
ppm													
Sc	13.40	13.80	11.70	17.16	17.10	16.20	16.60	16.50	15.50	4.93	4.68	4.69	4.70
V	201	193	168	229	159	127	122	135	134	55	60	53	52
Cr	15.70	14.50	68.10	86.72						26.40	23.20		
Co	24.40	25.00	22.80	25.20	34.10	35.80	35.90	32.30	30.00	8.29	8.28	7.95	7.99
Ni	23.30	23.60	44.00	23.76						23.40	21.20		
Cu	28.40	29.40	35.30	8.75	35.00	35.90	32.40	45.20	48.20	12.10	7.55	16.10	11.20
Zn	152	153	118	78						57	57		
Ga	22.20	22.20	20.70	23.62						19.10	19.20		
Rb	40	44	62	24	98	102	108	91	64	85	88	84	108
Sr	1426	1436	767	1466	779	1099	1077	1060	956	1007	897	983	1246
Y	19.10	19.70	15.20	20.20	16.90	14.60	14.80	16.50	16.40	10.10	9.97	9.12	9.14
Zr	223	212	213	223	208	191	186	209	213	208	210	206	204
Nb	17.60	18.80	20.30	17.15	6.93	8.83	8.62	8.41	8.03	7.39	7.24	7.48	7.16
Sb	0.07	0.05	0.49							0.14	0.15		
Cs	0.26	0.28	1.18	2.33	5.40	7.25	7.94	6.28	3.89	3.49	3.02	2.65	3.60
Ba	2062	2094	1187	1407	1387	1354	1437	2416	1862	2517	2232	2480	2454
Hf	5.47	5.76	5.57	4.90	4.70	4.19	4.20	4.71	4.76	5.74	5.66	4.91	4.83
Ta	0.96	0.96	1.15	0.65	0.37	0.63	0.68	0.53	0.44	0.47	0.44	0.51	0.50
Pb	29.60	25.60	12.70	5.69	15.80	46.00	27.50	26.90	26.30	71.50	63.60	45.60	61.80
Th	3.16	3.38	3.65	2.51	10.40	10.40	10.30	11.80	12.00	16.70	16.50	14.60	14.20
U	0.67	0.70	1.05	0.54	2.19	2.06	2.09	2.10	2.14	2.85	3.34	3.37	3.61
La	80.20	80.80	58.60	67.20	73.80	62.30	62.00	72.90	73.20	83.20	81.60	67.70	65.60
Ce	128	133	103	145	154	127	126	149	148	127	124	128	126
Pr	17.40	17.20	13.50	16.12	18.10	15.20	15.10	18.00	18.00	15.60	14.70	13.60	13.00
Nd	67.60	68.00	51.00	62.84	65.80	62.10	60.70	71.00	69.50	55.10	52.40	48.50	46.40
Sm	9.71	9.80	7.54	9.41	10.80	9.38	9.42	11.30	11.00	7.72	7.27	6.76	6.63
Eu	3.37	3.37	2.35	3.15	3.02	2.73	2.75	3.32	3.07	2.61	2.42	2.21	2.19
Gd	8.37	8.17	6.29	9.60	8.17	7.37	7.37	8.65	8.59	5.90	6.40	5.02	4.95
Tb	1.04	1.13	0.85	0.97	0.88	0.80	0.80	0.94	0.92	0.68	0.69	0.49	0.48
Dy	4.76	5.00	3.80	4.35	3.59	3.34	3.34	3.80	3.74	2.69	2.82	1.92	1.86
Ho	0.75	0.73	0.57	0.74	0.62	0.59	0.59	0.66	0.64	0.39	0.35	0.33	0.33
Er	2.12	2.19	1.63	2.21	1.52	1.43	1.44	1.59	1.55	1.17	1.15	0.86	0.85
Tm	0.26	0.27	0.21	0.28	0.21	0.21	0.21	0.23	0.22	0.15	0.16	0.13	0.13
Yb	1.63	1.62	1.23	1.76	1.27	1.27	1.25	1.35	1.34	0.92	0.97	0.81	0.79
Lu	0.23	0.24	0.19	0.24	0.19	0.19	0.19	0.21	0.20	0.13	0.14	0.12	0.12

* Ji et al. (2017).

characteristics of the magma sources, we adopt $\varepsilon_{Nd}(t) = \varepsilon_{Nd}(0.2\ Ga)$. Both rock types have indistinguishable Nd–Hf isotopic compositions, with $\varepsilon_{Nd}(t)$ values of −11.3 to −10.2 and $\varepsilon_{Hf}(t)$ values of −16.3 to −12.5, respectively. The one-stage Nd model age (T_{DM1}) and Hf model age (T_{DM1}) for the lamprophyres and quartz monzonite porphyries range from 1.45 to 1.52 Ga and 1.47 to 1.53 Ga, respectively. These Mesoproterozoic model ages do not correlate well with the Archean–Paleoproterozoic major crustal growth events or other known lithotectonic events in the NCC (Zhao and Zhai, 2013). Instead, they suggest that the parental magma was derived from mixed sources including Archean–Paleoproterozoic components as well as at least one younger depleted source. The"calculated" Hf isotope values for the lamprophyres and quartz monzonite porphyries (−18.8 to −16.3), determined using the relation $\varepsilon_{Hf}(t) = 1.55 \times \varepsilon_{Nd}(t) + 1.21$ (Vervoort et al., 2011), are in good agreement with the measured whole-rock Hf isotopic values for these samples (Fig. 5a).

5. Discussion

5.1. *Geochronological framework for northwestern Beijing: An exemplar of the northern NCC*

Previous studies have indicated that the Archean basement, represented by the Miyun Group, was widely distributed across northern Beijing. This interpretation was primarily based on its relationship with the country rocks in lithostratigraphy, single-grain dissolution zircon U–Pb ages and Sm–Nd whole-rock/mineral isochron ages (2500–3000 Ma; BBGMR, 1991; Jing and Guan, 1999). Some of these units were previously considered Mesoarchean to Neoarchean lithological assemblages within the northern NCC. However, recent high-precision dating has revealed that the Mesoarchean basement is not as widely distributed across the NCC as previously thought. Such basement rocks have only been identified in areas such as Anshan, Qingyuan, Lushan, Huashan, Eastern Hebei, and Eastern Shandong (Jahn et al., 2008; Li et al., 2020; Liou et al., 2019; Liu et al., 2009; Wan et al., 2007, 2015; Xie et al.,

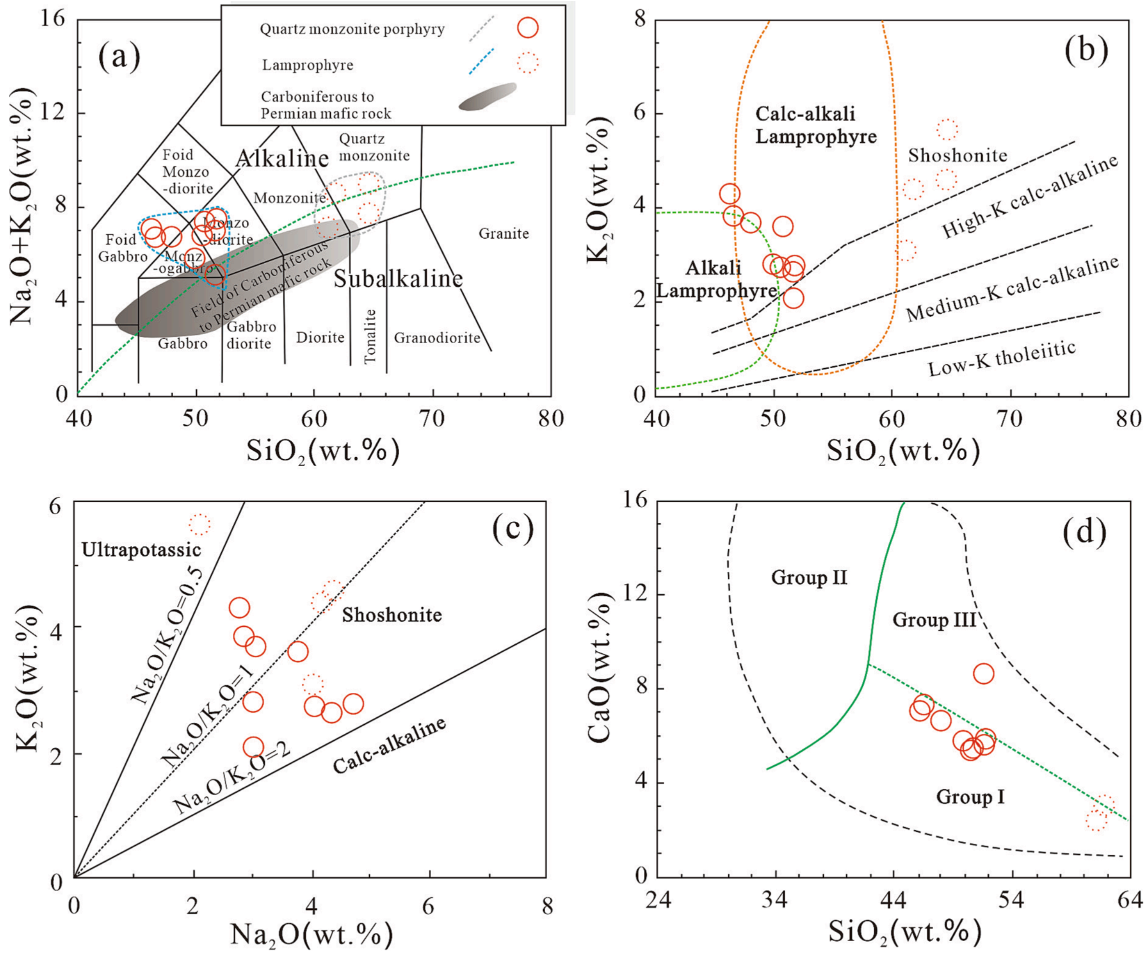

Fig. 6. Diagrams of (a) total alkalis versus SiO_2 (Irvine and Baragar, 1971; Middlemost, 1994), (b) K_2O versus SiO_2 (Rock, 1987), (c) K_2O versus Na_2O (Le Maitre, 2002), (d) CaO versus SiO_2, subdividing the lamprophyres into Groups I, II, and III (Foley et al., 1987; Miller et al., 1999). Geochemical data of Late Carboniferous to Early Permian hornblende gabbros are from Zhang et al. (2009a–c). Red solid circle and dashed circle represent Late Triassic lamprophyre and quartz monzonite porphyry sills in northwestern Beijing, northern NCC, respectively. (For interpretation of the references to color in this figure legend, the reader is referred to the web version of this article.)

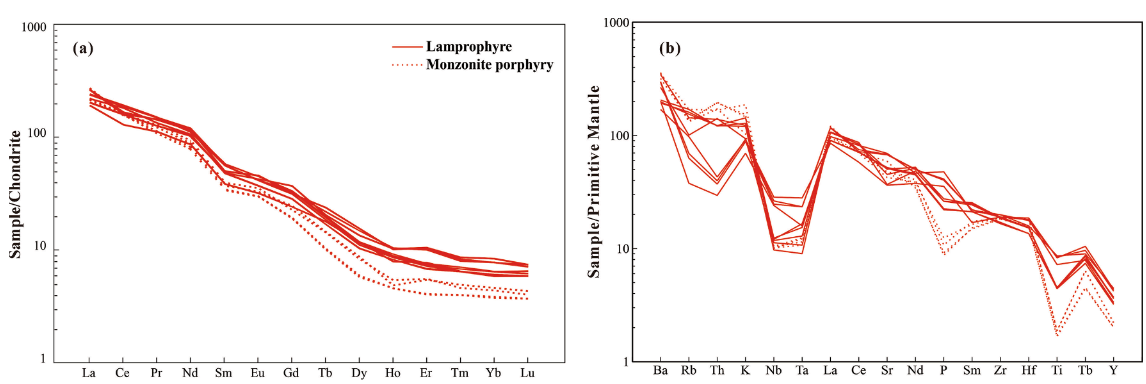

Fig. 7. (a) Chondrite-normalized REE patterns and (b) primitive mantle-normalized spider diagrams of Late Triassic lamprophyre and quartz monzonite porphyry sills in northwestern Beijing, northern NCC. Normalization values are from Sun and McDonough (1989).

2014). Therefore, the presence of Mesoarchean lithological assemblages within the Miyun Group remains uncertain and requires confirmation. As discussed above, most of the zircon grains from the granitic gneiss (Sample 19HY1-9), characterized by striped absorption and oscillatory growth zoning (Fig. 3a) and high Th/U ratios (>0.4), are of magmatic origin (Corfu et al., 2003; Pupin, 1980). Although three zircons, older than 2.7 Ga, were identified in this study, the emplacement age of the protolith can be constrained to 2.5 Ga (Fig. 4a). The integration of unpublished data from the vicinity with existing reliable geochronological data on the Miyun Group (including the data presented in this study) indicates that no rocks with Mesoarchean ages up to 3.0 Ga are present. Instead, the basement primarily formed during the Late Neoarchean, reflecting the Late Neoarchean tectono-thermal evolution of the eastern NCC (Zhao and Zhai, 2013). Similar cases have been identified in the

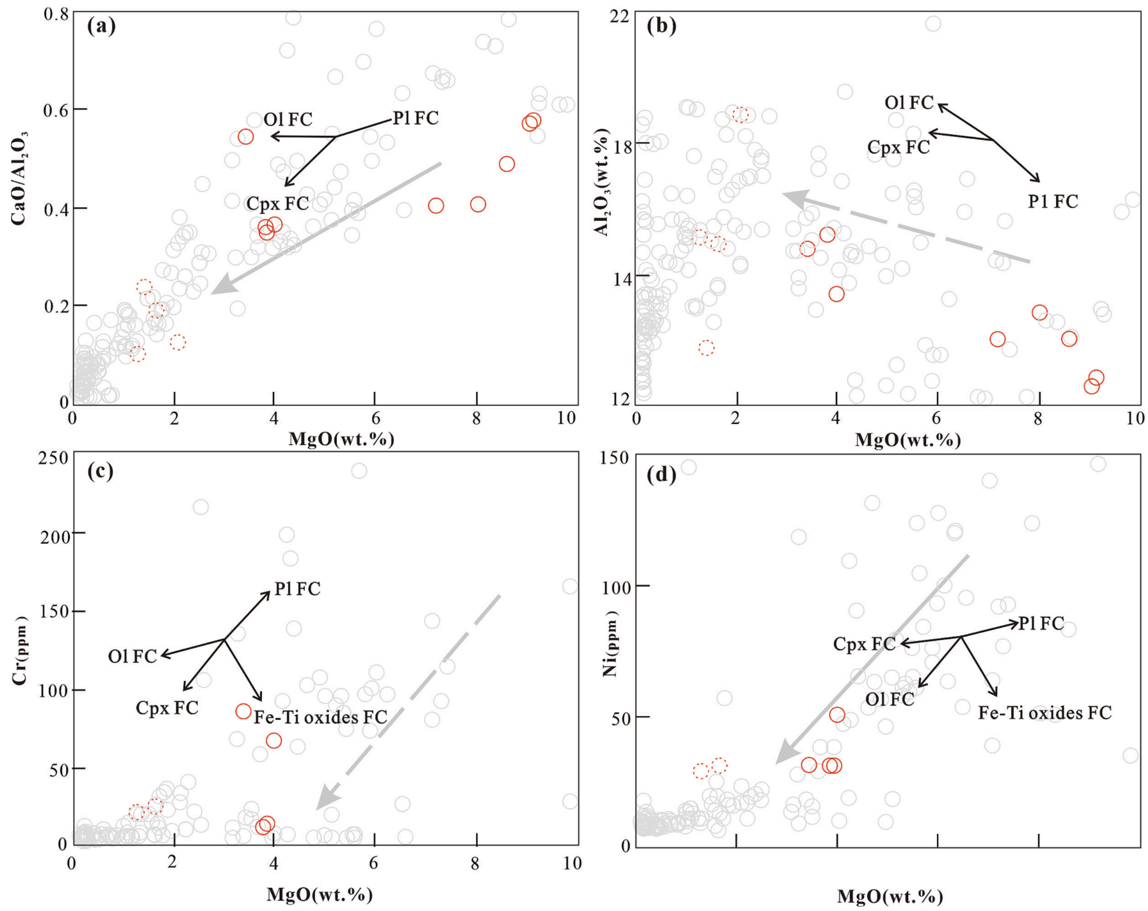

Fig. 8. Harker diagrams of selected major contents of Late Triassic lamprophyre and quartz monzonite porphyry sills in northwestern Beijing, northern NCC. The grey solid circle represents Late Triassic intrusions at other localities along the northern margin of the NCC (Zhang and Yang, 2007, 2009a–c, 2012; Tian et al., 2007; Wang et al., 2021 and references therein).

vicinity of Beijing, including eastern Liaoning and eastern Hebei (Duan et al., 2022; Li and Wei, 2017; Li et al., 2019, 2024; Yang et al., 2009), where Neoarchean basement rocks are prevalent, but Mesoarchean rocks are rare. The Late Neoarchean basement in northern Beijing is overlain by a thick sequence of unmetamorphosed Meso-Neoproterozoic (Changcheng, Jixian, and Qingbaikou Groups) marine clastic and carbonate platform sediments (HBGMR, 1989; Gao et al., 2008; Zhang et al., 2009a,b) (Fig. 1b and c). Deposition of the Changcheng Group began at approximately 1.8 Ga or earlier, followed by the Jixian Group at about 1.6 Ga and the Qingbaikou Group at around 1.4 Ga (Gao et al., 2008; Lu et al., 2008; Wan et al., 2011). To date, no Paleoproterozoic or Neoproterozoic magmatism has been identified in the region, although Paleoproterozoic magmatism is widespread in the Trans-North China Orogen and the Jiao–Liao–Ji Belt (e.g., Peng et al., 2017; Su et al., 2018; Zhao et al., 2005). The northern NCC remained tectonically stable until the Paleozoic (Zhu et al. 2012), when Late Paleozoic to Early Mesozoic mafic–ultramafic complexes were emplaced along its northern margin during the southward subduction of the Paleo-Asian oceanic plate (Zhang et al., 2014). The Late Triassic intrusions, including the *ca.* 220–230 Ma lamprophyre (Fig. 2e), quartz monzonite porphyry sills (Fig. 2g), and the 206 Ma aplite dykes (Ji et al., 2017) (Fig. 2i), likely mark the onset of the destruction of the NCC along its northern and eastern margins (Zhang et al., 2009a; Yang et al., 2007b, 2008, 2009). This destruction subsequently spread to the interior of the craton, with the peak destruction occurring during the Late Cretaceous, as evidenced by the emplacement of 130 Ma diabase dikes in northwestern Beijing (Fig. 2k). Additionally, widespread crust-derived felsic magmatism and large-scale ductile deformation during this time (Wu et al., 2019) further support this interpretation.

By integrating unpublished data with reliable geochronological studies, the evolution of northwestern Beijing, as a representative region of the northern NCC, can be subdivided into the following episodes: Late Neoarchean magmatism, Meso-Neoproterozoic to Paleozoic sedimentation, Late Triassic post-collisional magmatism, and Late Cretaceous regional magmatism across the entire NCC (Wu et al., 2019; Zhao and Zhai, 2013) (Fig. 1c).

5.2. *Petrogenesis of Late Triassic lamprophyres and quartz monzonite porphyries in northwestern Beijing*

The Late Triassic lamprophyres and quartz monzonite porphyries in northwestern Beijing, northern NCC, exhibit a wide range of whole-rock major and trace element compositions, along with a decoupling between whole-rock Nd–Hf and zircon Lu–Hf isotopic ratios (Supplementary Figs. 1 and 2; Tables 2–4). These data preclude the possibility of simple crystal-liquid fractionation from a relatively homogeneous pristine source to generate the entire suite. The key issue is whether they were derived from multiple magma sources, generated by complex petrogenetic processes, affected by post-magmatic processes, or a combination of these factors.

5.2.1. *Post-magmatic process*

The lamprophyres experienced weak to moderate alteration as evidenced by their relatively high loss on ignition (LOI) values (1.57–8.63 wt%; Table 3), whereas the quartz monzonite porphyries did not. Petrographic observations of the lamprophyres also reveal partial

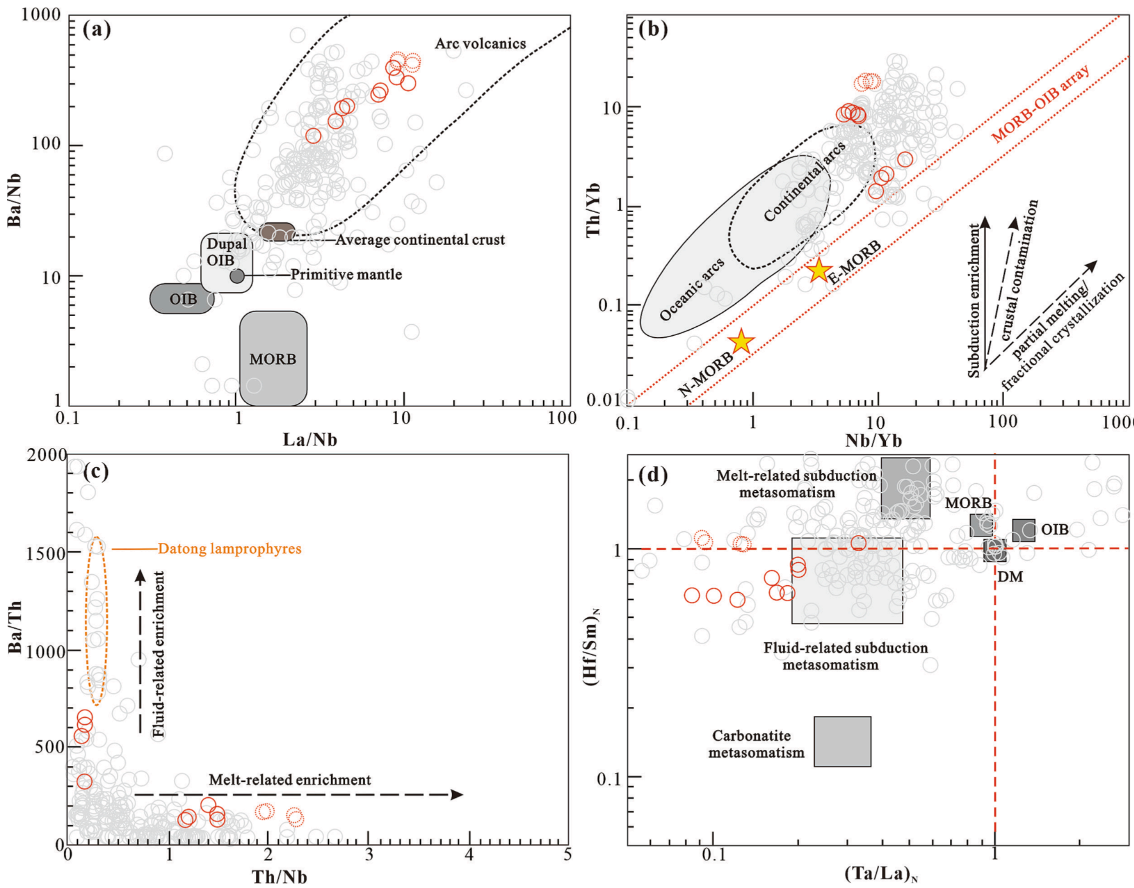

Fig. 9. Trace element diagrams of (a) Ba/Nb versus La/Nb, (b) Th/Yb versus Nb/Yb (Pearce, 2008; Pearce and Peate, 2005; Pearce et al., 2005), (c) Ba/Th versus Th/Nb (Choi et al., 2020; Johnson and Plank, 2000), and (c) $(Hf/Sm)_N$ versus $(Ta/La)_N$ (La Flèche et al., 1998).

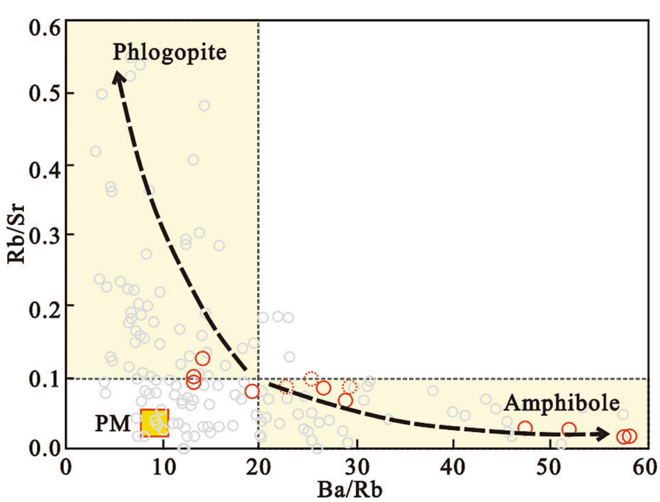

Fig. 10. Rb/Sr versus. Ba/Rb diagram (Furman and Graham, 1999).

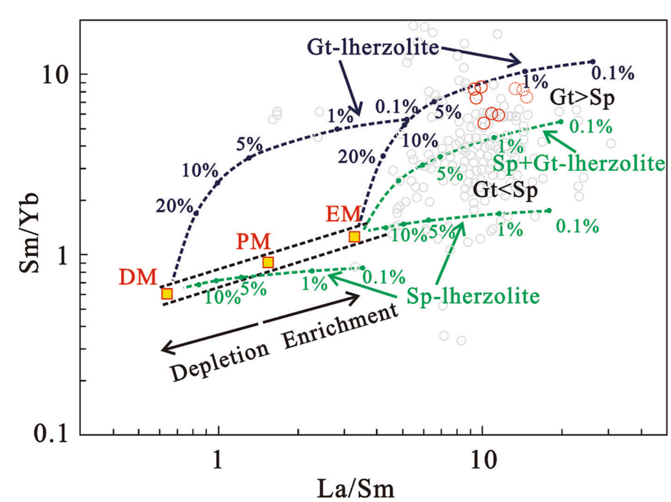

Fig. 11. Sm/Yb versus La/Sm diagram (Aldanmaz et al., 2000).

replacement of hornblendes by chlorite (Fig. 2f). However, it is widely accepted that FeO_{tot}, Al_2O_3, CaO, MgO, REEs and HFSEs (e. g., Nb, Ta, Th and Y) are relatively immobile during low-temperature alteration (Beswick, 1982; Barnes et al., 1985; Taylor and McLennan, 1995). The strong correlation of these elements with SiO_2 indicates their weak mobility (Supplementary Fig. 1). Moreover, the major and trace element contents and their ratios in the lamprophyres show systematic co-variations with MgO or SiO_2 (Supplementary Figs. 1 and 2; Table 3), suggesting an isochemical behavior during post-magmatic processes. In addition, the trace element patterns of the lamprophyres or quartz monzonite porphyries are comparable, as evidenced by the absence of Ce anomalies (Fig. 7a), which highlights their geochemical peculiarities. Sm–Nd and Lu–Hf isotopic systems are generally robust and remain unaffected even under intense metamorphic conditions (Barovich and Patchett, 1992; Chen and Jahn, 2002; Kemp and Hawkesworth, 2006). The samples exhibit limited variations in $^{147}Sm/^{144}Nd$ and $^{176}Hf/^{177}Hf$ ratios, and their whole-rock $\varepsilon_{Nd}(t)$ and $\varepsilon_{Hf}(t)$ values do not correlate with LOI (Table 3), further indicating that they were not significantly

Table 4
Whole-rock Nd and Hf isotope compositions.

Sample No.	Sm (ppm)	Nd (ppm)	$^{147}Sm/^{144}Nd$	$^{143}Nd/^{144}Nd$	2σ	$\varepsilon_{Nd}(0)$	$f_{Sm/Nd}$	$\varepsilon_{Nd}(T)$ (220 Ma)	T_{DM} (Ga)	Lu (ppm)	Hf (ppm)	$^{176}Lu/^{177}Hf$ Ratio	$^{176}Hf/^{177}Hf$ Ratio	2σ	$(^{176}Hf/^{177}Hf)_i$ Ratio	$\varepsilon_{Hf}(0)$	$\varepsilon_{Hf}(t)$	2σ	T_{DM1} (Ma)	T_{DM2} (Ma)	$f_{Lu/Hf}$
Triassic quartz monzonite porphyry																					
A-1-1	7.72	55.10	0.0847	0.511922	0.000004	−14.0	−0.57	−10.8	1.45	0.13	5.74	0.003	0.282241	0.000006	0.282228	−18.8	−14.4	0.2	1.51	2.15	−0.91
Triassic lamprophyre																					
A-2-1	9.71	67.60	0.0868	0.511899	0.000004	−14.4	−0.56	−11.3	1.50	0.23	5.47	0.006	0.282305	0.000005	0.282281	−16.5	−12.5	0.2	1.53	2.04	−0.82
B-2-1G	9.80	68.00	0.0871	0.511900	0.000004	−14.4	−0.56	−11.3	1.50	0.24	5.76	0.006	0.282312	0.000007	0.282312	−16.3	−16.3	0.2	1.52	2.11	−0.83
B-3-1G	7.54	51.00	0.0894	0.511910	0.000004	−14.2	−0.55	−11.2	1.52	0.19	5.57	0.005	0.282312	0.000006	0.282312	−16.3	−16.3	0.2	1.47	2.11	−0.86

Note: $\varepsilon_{Nd} = ((^{143}Nd/^{144}Nd)_s/(^{143}Nd/^{144}Nd)_{CHUR} - 1) \times 10{,}000$, $f_{Sm/Nd} = (^{147}Sm/^{144}Nd)_s/(^{147}Sm/^{144}Nd)_{CHUR} - 1$, $(^{143}Nd/^{144}Nd)_{CHUR} = 0.512638$, and $(^{147}Sm/^{144}Sm)_{CHUR} = 0.1967$. The model ages were calculated using a linear isotopic ratio growth equation: $T_{DM} = 1/\lambda \times \ln(1 + ((^{143}Nd/^{144}Nd)_s - 0.51315)/((^{147}Sm/^{144}Nd)_s - 0.2137))$.

influenced by post-magmatic alteration. Therefore, the geochemical and isotopic variations observed in these rocks are more likely attributable to petrogenetic processes or the nature of their mantle sources. Importantly, the sampling approach was designed to exclude lamprophyres and quartz monzonite porphyries containing veinlets (e.g., those with carbonate alteration or silicification), ensuring that such features did not affect the geochronological, geochemical, or isotopic analyses.

5.2.2. *Petrogenetic processes: crustal assimilation and fractional crystallization*

Mantle-derived magmas undergo various transcrustal processes before reaching the shallow crust, including fractional crystallization, crustal assimilation, and magma mixing (Handley et al., 2008; Li et al., 2021a,b; Liu et al., 2014). Among the multiple groups of zircon grains in the lamprophyres, no inherited zircon cores were identified, but older zircon xenocrysts of different ages were recognized (Figs. 3 and 4). This possibly reflects variable crustal assimilation during magma ascent. Reactions between mafic to intermediate magma and its wall rocks (e.g., Neoarchean metamorphic basement (19HY1-9) or Mesoproterozoic cover) might contribute to geochemical and isotopic variations during magma crystallization. Accordingly, it is essential to evaluate the effects of crustal assimilation, highlighting the following three aspects. First, the homogeneous and unradiogenic whole-rock Hf–Nd isotopes (Fig. 5), and the absence of significant changes in whole-rock ε_{Nd}(t) and ε_{Hf}(t) values for the Late Triassic lamprophyres and quartz monzonite porphyries, suggest that crustal assimilation was minor or insignificant. Second, crustal assimilation is expected to result in negative Nb–Ta anomalies relative to LILEs and LREEs, as well as positive Zr–Hf anomalies due to the enrichment of Zr and Hf in crustal materials (Zhao and Zhou, 2007). The negative Zr anomalies, coupled with positive Hf anomalies in the lamprophyres, along with Nb–Ta depletion, are consistent with the isotopic evidence (Fig. 7b). Third, the low Th/Ce (0.02–0.08) and Th/La (0.04–0.17) ratios of the lamprophyres further confirm the low level of crustal assimilation, as continental crust typically exhibits higher Th/Ce (~0.15, Taylor and McLennan, 1995) and Th/La (~0.30, Plank, 2005), whereas mantle-derived magmas display lower Th/Ce (0.02–0.05) and Th/La (~0.12) ratios (Sun and McDonough, 1989). However, it is important to note that fractional crystallization may influence these elemental ratios, making this conclusion less definitive. Consequently, assimilation and fractional crystallization (AFC) processes must be considered. To minimize the effect of fractional crystallization, Ba, Th, and Nb are treated as fractionation indices due to their incompatibility during fractional crystallization (Bohrson and Spera, 2001; DePaolo, 1981; Ersoy and Helvacı, 2010; Wu et al., 2021). The results of the AFC model are inconsistent with negative correlations between Ba–Nb and Th–Nb (Supplementary Fig. 3), suggesting that the effects of crustal assimilation were limited. Additionally, correlations among selected trace element ratios, which are sensitive to crustal assimilation, show no significant trends in variation diagrams such as Sm/Nd versus Nb/La, La/Sm versus Nb/La, and Nb/U versus SiO_2/MgO. These observations exclude significant bulk assimilation of crustal materials and confirm that these ratios reflect petrogenetic processes.

Of particular note, the lamprophyres exhibit systematic variations in the Harker diagrams (Supplementary Figs. 1 and 2), suggesting that they are likely products of differentiation from a mafic parental magma. This interpretation is supported by the low but variable $Mg^{\#}$ values ranging from 40 to 71 (Table 3), which is lower than the $Mg^{\#}$ (~72) expected for primitive melt compositions in equilibrium with a peridotite source (Niu and O'Hara, 2008). This further confirms that the lamprophyre parental melts underwent a certain degree of crystal fractionation. Positive correlations between MgO and CaO, as well as MgO and Ni, suggest that olivine and/or clinopyroxene were likely the primary fractionating phases (Fig. 8a and d). While the correlations between MgO and Al_2O_3 with Cr are less pronounced, they still demonstrate trends associated with the fractional crystallization of olivine and clinopyroxene (Fig. 8b and c). However, the fractional crystallization of olivine is inconsistent with its absence in the rocks and the lack of correlations between MgO and CaO (Supplementary Fig. 2). Similarly, the absence of Eu anomalies (Fig. 7a) and the negative correlations between MgO and Al_2O_3 (Fig. 8b) argue against significant plagioclase fractionation. Fractionation of apatite and Fe–Ti oxides likely played a role, as indicated by the positive correlation between P_2O_5 and TiO_2 (Table 3). The lack of correlations between MgO and V, as well as SiO_2 and FeO suggests a minimal contribution from amphibole and biotite as cumulate phases, which is also confirmed by petrographic observations. Thus, the geochemistry of the studied samples was primarily controlled by their mantle sources rather than by magmatic differentiation.

5.2.3. Magma mixing: multiple versus singular magma source

The origin of lamprophyric magmas remains enigmatic (e.g., Aghazadeh et al., 2015; Casetta et al., 2019; Yang and Jiang, 2018). Proposed models include: (1) assimilation of mafic alkaline magmas with continental crustal materials or melts (Prelević et al., 2004, 2008; Rock, 1987), (2) partial melting of metasomatized and enriched mantle (e.g., Avanzinelli et al., 2009; Conticelli and Peccerillo, 1992; Fowler and Henney, 1996; Gibson et al., 1995; McKenzie, 1989; Owen, 2008; Prelević et al., 2004; Thompson et al., 1990; Wallace et al., 1992; Zhang et al., 2003), and (3) mixing of upwelling basaltic magma with varying amounts of ultrapotassic melts, which generally originate in the lithospheric mantle and are associated with heating and/ or thinning of the subcontinental lithospheric mantle (Thompson et al., 1990; Yang and Jiang, 2018; Zhang et al., 2023). The existing isotopic and geochemical data favor an interaction between the asthenosphere and lithospheric mantle, but contradictions with other models remain unresolved.

Lamprophyres in northwestern Beijing, which are characterized by relatively low SiO_2 and high MgO, MnO, CaO, Cr and Ni concentrations (Fig. 6; Table 3) are distinct from crust-derived melts (Frey and Prinz, 1978; Rudnick and Gao, 2003). These features suggest their derivation primarily from an ultramafic source (Carmichael et al., 1996). The compositional similarities in whole-rock Hf–Nd isotopes and trace elements between the lamprophyres and quartz monzonite porphyries suggest a shared source (Figs. 5, 7; Table 4). Model (1) is inconsistent with the relatively homogeneous whole-rock $\varepsilon_{Nd}(t)$ and $\varepsilon_{Hf}(t)$ values, as crustal assimilation during magma ascent would typically result in isotopic variations. This explanation also conflicts the evidence for only minor crustal assimilation. The relatively high K_2O contents, alkali enrichment (Fig. 6), and low $\varepsilon_{Nd}(t)$ and $\varepsilon_{Hf}(t)$ values (Fig. 5a) of the lamprophyres and quartz monzonite porphyries suggest their derivation from partial melting of an enriched domain in the lithospheric mantle. Such enrichment could be attributed due to mantle plume underplating, upwelling of asthenosphere during mantle stretching, and/or recycling of subducted oceanic or continental crust (Chakrabarti et al., 2009; Tappe et al., 2007; Willbold and Stracke, 2006, 2010). The lamprophyres exhibit high Ba/Nb ratios (58–287), plotting within the arc field on a Ba/Nb versus La/Nb diagram (Fig. 9a), and Th/Yb ratios (17–80) at relatively constant Nb/Yb ratios above the mid-ocean ridge basalt–ocean island basalt (MORB–OIB) array (Pearce, 2008; Pearce and Peate, 1995; Pearce et al., 2005) (Fig. 9b). These rocks also display subduction-related geochemical features, including crust-like trace element patterns (Fig. 7; enrichment in LILEs such as K, Ba and Sr; and depletion in HFSEs, such as Nb, Ta and Ti) and unradiogenic whole-rock Hf and Nd isotope ratios (Fig. 5). These geochemical signatures exclude their derivation from MORB- or OIB-like magmas, ruling out convective asthenosphere or mantle plume sources (Fig. 7; Sun and McDonough, 1989). The enrichment of the subcontinental lithospheric mantle source is unlikely to be attributed to a mantle plume or upwelling asthenosphere during lithospheric stretching, as the lamprophyres exhibit strong Nb and Ta depletion, which contrasts with features of sources metasomatized by asthenosphere (Tappe et al., 2007). Instead, these characteristics provide compelling evidence for the recycling of crustal components into the mantle source via subduction zones (e.g., Avanzinelli et al., 2009; Conticelli and Peccerillo 1992; Conticelli et al., 2002, 2011, 2015; Prelević et al., 2008, 2012; Tommasini et al., 2011). This evidence supports a model in which the lamprophyres in Datong, near Beijing, were derived from magmas generated by partial melting of the subcontinental lithospheric mantle (Niu et al., 2017). These rocks are characterized by significant fractionation of LREEs over HREEs and are enriched in LILEs (Cs, Rb, and Ba) while being depleted in HFSEs (Nb, Ta, and Zr) (Fig. 7). These features are consistent with arc-type magmas (Fig. 8a). The lamprophyres in northwestern Beijing and Datong, along with other Late Triassic mafic rocks along the northern margin of the NCC, suggest a lithospheric mantle source that experienced melt- or fluid-related metasomatism during subduction (Fig. 9c; Choi et al., 2020; Johnson and Plank, 2000), possibly leading to first-order heterogeneity (Stracke, 2012). Notably, the lamprophyres in northwestern Beijing exhibit wide ranges of Th concentrations and variable Th/Nb and Ba/Th ratios, indicating the presence of recycled sediment in their mantle source as melts or aqueous fluids rather than as the result of carbonatite-related process (La Flèche et al., 1998) (Fig. 9d). In contrast, Datong potassic and ultrapotassic rocks show a dominant role of a melt-related metasomatic components, characterized by high but variable Ba/Th ratios and low Th/Nb ratios (Avanzinelli et al. 2009; Conticelli et al. 2015) (Fig. 9c).

Mantle metasomatism likely resulted in the formation of hydrous phases, such as amphibole, phlogopite and apatite in the mantle wedge above subduction zones (Ionov et al., 1997). These minerals, of metasomatic origin, are inferred to occur in the mantle source regions, consistent with the volatile-rich characteristics of the lamprophyres (Batki et al., 2014; Foley, 1992). Since Rb is preferentially sequestered in phlogopite relative to Sr, and Ba partitions more strongly than Rb into the amphiboles (LaTourrette et al., 1995), melts in equilibrium with phlogopite are expected to have higher Rb/Sr ($>$ 0.1) and lower Ba/Rb ($<$20) ratios (Furman and Graham, 1999). The lamprophyres in northwestern Beijing have low Rb/Sr ratios (0.02–0.13, averaging 0.08) and high Ba/Rb ratios (13.27–57.95, averaging 29.22), suggesting that amphibole predominates over phlogopite in their melting source (Fig. 10). Other Late Triassic mafic rocks show a large range of Rb/Sr and Ba/Rb ratios, indicating heterogeneous metasomatism and variable distributions of amphibole and phlogopite in their mantle sources (Foley, 1992) (Fig. 10). This observation of hydrous phases is further supported by K_2O enrichment and elevated K_2O/Na_2O ratios (0.6–1.5) in the samples, as partial melting of amphibole-bearing mantle generates shoshonitic to ultrapotassic melts (Wilson and Downes, 1991), which are responsible for alkaline magma genesis (Luhr, 1997; Luhr et al., 1989). The concentration of K in equilibrium partial melts remains constant at over 40 000 ppm when K is hosted in the mantle phlogopite, but only 7000 ppm when hosted in mantle amphibole (Spath et al., 1996). The K contents of the lamprophyres (17727–36383 ppm, averaging 26837 ppm) suggest contributions from both amphibole and phlogopite in the mantle source.

In addition to amphibole and phlogopite, the mineralogy and partial melting processes can be further constrained using REE ratios (Aldanmaz et al., 2000; Li and Chen, 2014; Li and Wei, 2017). Highly incompatible elements such as La and less incompatible elements like Sm are relatively unaffected by the source mineralogy variations (e.g., garnet or spinel), while Yb is compatible with garnet but not with clinopyroxene or spinel. Thus, the La/Sm ratio reflects the bulk chemical composition of the source, whereas the Sm/Yb ratio constrains the source mineralogy (Aldanmaz et al., 2000 and references therein). The lamprophyres from northwestern Beijing have higher La/Sm ratios than those generated by direct melting of a depleted mantle, even at very small degrees of partial melting ($<$0.1 %), consistent with an origin in an enriched mantle rather than the convective asthenosphere (as noted above). On a Sm/Yb versus La/Sm diagram (Fig. 11), the samples exhibit Sm/Yb ratios higher than the spinel lherzolite melting curve but mostly lower than the garnet lherzolite melting trend, plotting slightly above the spinel + garnet lherzolite (spinel: garnet = 1:1) melting curve. This suggests a mantle source composed of spinel-bearing garnet lherzolite.

Modeling indicates that 1%–5% partial melting of such a mantle source is required to generate the parental magma of the northwestern Beijing lamprophyres (Fig. 11), corresponding to depths of ~ 70–80 km, consistent with the garnet-spinel transition zone in enriched lherzolitic mantle rocks (Duggen et al., 2005; Klemme and O'Neill, 2000; Menzies, 1989).

In light of the above discussion, the lamprophyres in northwestern Beijing likely originated from an enriched lithospheric mantle source in the spinel-garnet transition zone, with significant contributions from amphibole and phlogopite. Recent studies suggest that zircon Hf isotopic compositions may be more effective than whole-rock Hf and Nd isotopes in elucidating mantle sources and transcrustal processes in magmatic rocks (e.g., Griffin et al., 2002). The radiogenic zircon $\varepsilon_{Hf}(t)$ values of the Late Triassic lamprophyres in northwestern Beijing (up to +8.9) negate the their sole derivation from an enriched lithospheric mantle source, supporting Model (2) (Fig. 5a). This requires an exotic mantle component. The decoupling of whole-rock Nd and Hf isotopic compositions from zircon Hf isotopes reflects differences in closure temperatures (Fig. 5b). Zircon Hf isotopes record early magma evolution, whereas whole-rock isotopic compositions represent late-stage mixing during decreasing magma temperatures. The significantly positive zircon $\varepsilon_{Hf}(t)$ values (+8.9) and young Hf model ages (T_{DM} = 0.5 Ga) suggest contributions from young mantle domains depleted in Hf. This contrasts with the ancient enriched lithospheric mantle inferred from negative whole-rock Hf and Nd isotopes. The Late Triassic ultramafic–mafic rocks and alkaline complexes in the northern NCC show trends consistent with asthenosphere–lithosphere interaction, suggesting asthenospheric upwelling contributed to magma source mixing (Ma et al., 2014; Smith et al., 1999; Sun and McDonough, 1989; Wang et al., 2005; Zhang and Sun, 2002) (Supplementary Fig. 4). Some mafic rocks even exhibit lower Nb/La ratios than magmas derived solely from the lithospheric mantle. The absence of a strong asthenospheric signal likely reflects the low proportion of convective mantle components in the magma source, which is sufficient to generate the arc-like geochemical characteristics of the lamprophyres (e.g., LILE enrichment, HFSE depletion, and fractionated REE patterns). Modeling suggests that incorporation of <20 % asthenospheric melts can successfully explain the average Nb/La ratio (0.18) of the lamprophyres in northwestern Beijing (Supplementary Fig. 4), assuming primitive mantle melts have Nb/La = 1.39 and La/Yb = 1.04 (Sun and McDonough, 1989), while Mesozoic lithospheric mantle melts have Nb/La = 0.10 and La/Yb = 30.70 (Zhang and Sun, 2002; Wang et al., 2005; Ma et al., 2014).

6. Tectonic implications

There is a consensus on the tectonic evolution of the northern margin of the NCC from the early Paleozoic to the early Mesozoic (Zhang et al., 2014; Wu et al., 2019). Specifically, the southward subduction of the Paleo-Asian oceanic slab beneath the NCC led to the formation of arc-accretionary series during the early Paleozoic (490–446 Ma; Xiao et al., 2003; Windley et al., 2007). This subduction persisted into the mid- to late Paleozoic, as evidenced by Late Paleozoic Andean-type continental arc magmatism with adakitic compositions along the northern margin of the craton (390–280 Ma; Zhang and Yang, 2007, 2009a). The cessation of subduction of the Paleo-Mongolian Ocean (a segment of the Paleo-Asian Ocean) beneath the northern margin of the craton can thus be constrained to around 280 Ma or later (Chen et al., 2000, 2009; Zhang et al., 2009a). The Late Permian–Middle Triassic K-rich and K-feldspar porphyritic calc-alkaline granitoids are interpreted as being emplaced in post-collisional or post-orogenic settings, such as the strongly deformed Late Permian Guanglingshan pluton along the Damiao-Guanglingshan shear zone (Zhang et al., 2009c). Subsequently, the Late Triassic geodynamics of the NCC were predominantly governed by a post-collisional regime following its amalgamation with neighboring blocks. This regime was characterized by a transition from compression-dominated to extension-dominated stress fields (Zhang et al., 2014). This shift to post-collisional extension is evidenced by Late Triassic detachment faults with E-W strikes, metamorphic core complexes, L-tectonites and isolated rift basins along the northern margin of the NCC (Davis et al., 2001, 2004; Meng et al., 2020; Zhang et al., 2014). This transition aligns with the classification of the lamprophyres in northwestern Beijing as a transitional type between Groups I (anorogenic lamproites) and III (orogenic ultrapotassic series), as recognized by Foley et al. (1987), based on their relatively high SiO_2 (>45 wt%) and low Al_2O_3 contents (mostly <8 wt%) (Fig. 6d). No mantle plume activity occurred during this period to drive extension (McKenzie and Bickle, 1988). Instead, the process likely involved the passive upwelling of asthenosphere, which experienced decompressional melting. The appearance of asthenosphere-derived magmas and the transition from lithospheric to asthenospheric mantle sources are regarded as key indicators of craton destruction (Wu et al., 2008; Xu et al., 2009). However, occurrences of asthenosphere-derived magmas in the Mesozoic NCC are rare. Evidence for asthenosphere–lithosphere interaction is limited to the geochemical characteristics of Triassic ultramafic–mafic rocks and alkaline complexes (Wang et al., 2021) (Supplementary Fig. 4), Sr–Nd–Hf isotope compositions from Middle–Late Triassic alkaline complexes (Zhang et al., 2012), and radiogenic zircon Hf isotope compositions. Late Triassic zircons with positive $\varepsilon_{Hf}(t)$ values from the lamprophyres, distinct from known igneous zircons in the NCC (Yang et al., 2006), suggest an exotic source beyond the ancient enriched lithospheric mantle, namely, a depleted asthenospheric mantle source. Yang et al. (2007b) similarly identified asthenospheric contributions in Late Triassic dyke swarms from the Liaodong Peninsula, northeastern China.

During the Late Triassic post-collisional extension, lithospheric thinning and passive upwelling of juvenile asthenosphere formed an east–west-trending alkaline/ultramafic magmatic belt along the northern margin of the NCC (Zhang et al., 2012). The asthenosphere likely penetrated the lithospheric mantle along fractures or weak zones, causing disintegration of the lithospheric mantle (Xu, 2001; Foley 2008). The upwelling hot asthenosphere induced partial melting of the enriched lithospheric mantle, forming Late Triassic ultramafic–mafic rocks and alkaline complexes along the northern margin of the NCC. This process, involving both energy and mass transfer, suggests that bottom-up thermal–mechanical erosion may have been a critical mechanism in craton destruction (Xu, 2001; Xu et al., 2004). Thus, the transition in mantle sources during the Late Triassic marks the onset of NCC destruction, while the Cretaceous period represents its peak. This is evidenced by the newly identified Late Triassic lamprophyre and quartz monzonite porphyry sills (235–220 Ma) and Early Cretaceous diabase dykes (*ca.* 120 Ma) from northwestern Beijing as presented in this study.

CRediT authorship contribution statement

Zhuang Li: Writing – review & editing, Writing – original draft, Data curation, Conceptualization. **Guochun Zhao:** Writing – review & editing, Data curation, Conceptualization. **Bin Chen:** Data curation, Conceptualization. **Mingshuo Qin:** Data curation, Conceptualization.

Declaration of competing interest

The authors declare that they have no known competing financial interests or personal relationships that could have appeared to influence the work reported in this paper.

Acknowledgements

Special thanks to the Editor-in-Chief Prof. Meifu Zhou, Associate Editor Prof. Huaiyu He, and two anonymous reviewers for their insightful comments that led to significant improvement in the manuscript. We are grateful to Dr. Hafiz Ur Rehman of Kagoshima University, and Dr. Chaokun Zhang, Dr. Jiahong Gao, and Dr. Rongbin Yang of

Peking University for their perceptive suggestions and careful corrections on preparing the manuscript for this paper. This work was supported financially by the National Natural Science Foundation of China (Grant Numbers: 42002238 and 41872057).

Appendix A. Supplementary data

Supplementary data to this article can be found online at https://doi.org/10.1016/j.jseaes.2025.106504.

Data availability

No data was used for the research described in the article.

References

Aghazadeh, M., Prelević, D., Badrzadeh, Z., Braschi, E., van den Bogaard, P., Conticelli, S., 2015. Geochemistry, Sr–Nd–Pb isotopes and geochronology of amphibole- and mica-bearing lamprophyres in northwestern Iran: implications for mantle wedge heterogeneity in a palaeo-subduction zone. Lithos 216–217, 352–369.
Aldanmaz, E., Pearce, J.A., Thirlwall, M.F., Mitchell, J.G., 2000. Petrogenetic evolution of late Cenozoic, post-collision volcanism in western Anatolia, Turkey. J. Volcanol. Geotherm. Res. 102, 67–95.
Amelin, Y., 2005. Meteorite phosphates show constant ^{176}Lu decay rate since 4557 million years ago. Science 310, 839–841.
Andersen, T., 2002. Correction of common lead in U–Pb analyses that do not report ^{204}Pb. Chem. Geol. 192, 59–79.
Andersson, T., Möller, C., Johansson, L., 2002. Zircon geochronology of migmatite gneisses along the mylonite zone (S Sweden): a major Sveconorwegian terrane boundary in the Baltic Shield. Precambr. Res. 114, 121–147.
Avanzinelli, R., Lustrino, M., Mattei, M., Melluso, L., Conticelli, S., 2009. Potassic and ultrapotassic magmatism in the circum-Tyrrhenian region: significance of carbonated pelitic vs. pelitic sediment recycling at destructive plate margins. Lithos 113, 213–227.
Baines, A.G., Cheadle, M.J., John, B.E., Grimes, C.B., Schwartz, J.J., Wooden, J.L., 2009. SHRIMP Pb/U zircon ages constrain gabbroic crustal accretion at Atlantis Bankon the ultraslow-spreading Southwest Indian Ridge. Earth Planet. Sci. Lett. 287, 540–550.
Barnes, S.J., Naldrett, A.J., Gorton, M.P., 1985. The origin of the fractionation of platinum-group elements in terrestrial magmas. Chem. Geol. 53, 303–323.
Barovich, K.M., Patchett, P.J., 1992. Behaviour of isotopic systematics during deformation and metamorphism: a Hf, Nd, and Sr isotopic study of mylonitized granite. Contrib. Mineral. Petr. 109, 386–393.
Batki, A., Pál-Molnár, E., Dobosi, G., Skelton, A., 2014. Petrogenetic significance of ocellar camptonite dykes in the Ditrău Alkaline Massif, Romania. Lithos 200–201, 181–196.
BBGMR (Beijing Bureau of Geology and Mineral Resources), 1991. Regional geology of Beijing Municipality. Geological Publishing House, Beijing, 11–21 (in Chinese with English abstract).
Belousova, E.A., Griffin, W.L., O'Reilly, S.Y., Fisher, N.I., 2002. Igneous Zircon: trace element composition as an indicator of source rock type. Contrib. Mineral. Petr. 143, 602–622.
Beswick, A.E., 1982. Some geochemical aspects of alteration and genetic relations in komatiitic suites. In: Arndt, N.T., Nisbet, E.G. (Eds.), Komatiites. George Allen and Unwin, London, pp. 283–308.
Blichert-Toft, J., Albarède, F., 1997. The Lu–Hf isotope geochemistry of chondrites and the evolution of the mantle-crust system. Earth Planet. Sci. Lett. 148, 243–258.
Bohrson, W.A., Spera, F.J., 2001. Energy-constrained open-system magmatic processes II: application of energy-constrained assimilation-fractional crystallization (EC–AFC) model to magmatic systems. J. Petrol. 42, 1019–1041.
Carlson, R.W., Pearson, D.G., James, D.E., 2005. Physical, chemical, and chronological characteristics of continental mantle. Rev. Geophys. 43, 1–24.
Carmichael, I.S.E., Lange, R.A., Luhr, J.F., 1996. Quaternary minettes and associated volcanic rocks of Mascota, western Mexico: a consequence of plate extension above a subduction modified mantle wedge. Contrib. Mineral. Petr. 124, 302–333.
Casetta, F., Ickert, R.B., Mark, D.F., Bonadiman, C., Giacomoni, P.P., Ntaflos, T., Coltorti, M., 2019. The alkaline lamprophyres of the Dolomitic Area (Southern Alps, Italy): Markers of the late Triassic change from orogenic-like to anorogenic magmatism. J. Petrol. 60, 1263–1298.
Chakrabarti, R., Basu, A.R., Santo, A.P., Tedesco, D., Vaselli, O., 2009. Isotopic and geochemical evidence for a heterogeneous mantle plume origin of the Virunga volcanics, Western rift, East African Rift system. Chem. Geol. 259, 273–289.
Chen, B., Jahn, B.M., 2002. Geochemical and isotopic studies of the sedimentary and granitic rocks of the Altai orogen of northwest China and their tectonic implications. Geol. Mag. 139, 1–13.
Chen, B., Jahn, B.M., Wilde, S., Xu, B., 2000. Two contrasting Paleozoic magmatic belts in northern Inner Mongolia, China: petrogenesis and tectonic implications. Tectonophysics 328, 157–182.
Chen, B., Jahn, B.M., Tian, W., 2009. Evolution of the Solonker suture zone: constraints from zircon U–Pb ages, Hf isotopic ratios and whole-rock Nd–Sr isotopic compositions of subduction- and collision-related magmas and forearc sediments. J. Asian Earth Sci. 34, 245–257.
Choi, E., Fiorentini, M.L., Giuliani, A., Foley, S.F., Maas, R., Taylor, W.R., 2020. Subduction-related petrogenesis of Late Archean calc-alkaline lamprophyres in the Yilgarn Craton (Western Australia). Precambrian Res 338, 105550.
Chu, N.C., Taylor, R.N., Chavagnac, V., Nesbitt, R.W., Boella, R.M., Milton, J.A., German, C.R., Bayon, G., Burton, K., 2002. Hf isotope ratio analysis using multi-collector inductively coupled plasma mass spectrometry: an evaluation of isobaric interference corrections. J. Anal. At. Spectrom. 17, 1567–1574.
Conticelli, S., Avanzinelli, R., Marchionni, S., Tommasini, S., Melluso, L., 2011. Sr–Nd–Pb isotopes from the Radicofani Volcano, Central Italy: constraints on heterogeneities in a veined mantle responsible for the shift from ultrapotassic shoshonite to basaltic andesite magmas in a post-collisional setting. Mineral. Petrol. 103, 123–148.
Conticelli, S., Avanzinelli, R., Ammannati, E., Casalini, M., 2015. The role of carbon from recycled sediments in the origin of ultrapotassic igneous rocks in the Central Mediterranean. Lithos 232, 174–190.
Conticelli, S., Peccerillo, A., 1992. Petrology and geochemistry of potassic and ultrapotassic volcanism in central Italy: petrogenesis and inferences on the evolution of the mantle sources. Lithos 28, 221–240.
Conticelli, S., D'Antonio, M., Pinarelli, L., Civetta, L., 2002. Source contamination and mantle heterogeneity in the genesis of Italian potassic and ultrapotassic volcanic rocks: Sr–Nd–Pb isotope data from Roman Province and Southern Tuscany. Mineral. Petrol. 74, 189–222.
Corfu, F., Hanchar, J.M., Hoskin, P.W.O., Kinny, P., 2003. Atlas of zircon textures. Rev. Mineral. Geochem. 53, 469–500.
Davis, G.A., Cong, W., Yadong, Z., Jinjiang, Z., Changhou, Z., Gehrels, G.E., 1998. The enigmatic Yinshan fold-and thrust belt of northern China: new views on its intraplate contractional styles. Geology 26, 43–46.
Davis, G., Xu, B., Zheng, Y.D., Zhang, W.J., 2004. Indosinian extension in the Solonker suture zone: the Sonid Zuoqi metamorphic core complex, Inner Mongolia, China. Earth Sci. Front. 11, 135–144.
Davis, G.A., Zheng, Y.D., Wang, C., Darby, B.J., Zhang, C.H., Gehrels, G., 2001. Mesozoic tectonic evolution of the Yanshan fold and thrust belt, with emphasis on Hebei and Liaoning Provinces, Northern China. Geol. Soc. Am. Memo. 194, 171–197.
Deng, J.F., Su, S.G., Niu, Y.L., Liu, C., Zhao, G.C., Zhao, X.G., Zhou, S., Wu, Z.X., 2007. A possible model for the lithospheric thinning of North China Craton: evidence from the Yanshanian (Jura-Cretaceous) magmatism and tectonic deformation. Lithos 96, 22–35.
DePaolo, D.J., 1981. Trace element and isotopic effects of combined wallrock assimilation and fractional crystallization. Earth Planet. Sci. Lett. 53, 189–202.
Diwu, C., Sun, Y., Wilde, S.A., Wang, H., Dong, Z., Zhang, H., Wang, Q., 2013. New evidence for ~4.45 Ga terrestrial crust from zircon xenocrysts in Ordovician ignimbrite in the North Qinling Orogenic Belt, China. Gondwana Res. 23, 1484–1490.
Duan, Z.Z., Wei, C.J., Li, Z., Zhang, C., 2022. Zircon U–Pb Dating and Metamorphism of granitoid gneisses and supracrustal rocks in Eastern Hebei, North China Craton. Minerals 12, 863.
Ducea, M., Saleeby, J., 1988. A case for delamination of the deep batholithic crust beneath the Sierra Nevada, California. Int. Geol. Rev. 40, 78–93.
Duggen, S., Hoernle, K., van den Bogaard, P., Garbe-Schönberg, D., 2005. Post-collisional transition from subduction-to intraplate-type magmatism in the westernmost Mediterranean: evidence for continental-edge delamination of subcontinental lithosphere. J. Petrol. 46, 1155–1201.
Ersoy, Y., Helvacı, C., 2010. FC–AFC–FCA and mixing modeler: a Microsoft® Excel©spreadsheet program for modeling geochemical differentiation of magma by crystal fractionation, crustal assimilation and mixing. Comput. Geosci. 36, 383–390.
Foley, S., 1992. Vein-plus-wall-rock melting mechanisms in the lithosphere and the origin of potassic alkaline magmas. Lithos 28, 435–453.
Foley, S.F., 2008. Rejuvenation and erosion of the cratonic lithosphere. Nat. Geosci. 1, 503–510.
Foley, S.F., Venturelli, G., Green, D.H., Toscani, L., 1987. The ultrapotassic rocks: characteristics, classification, and constraints for petrogenetic models. Earth Sci. Rev. 24, 81–134.
Fowler, M.B., Henney, P.J., 1996. Mixed Caledonian appinite magmas: implications for lamprophyre fractionation and high Ba–Sr granite genesis. Contrib. Mineral. Petr. 126, 199–215.
Frey, F.A., Prinz, M., 1978. Ultramafic inclusions from San Carlos, Arizona: petrologic and geochemical data bearing on their petrogenesis. Earth Planet. Sci. Lett. 38, 129–176.
Furman, T., Graham, D., 1999. Erosion of lithospheric mantle beneath the East African Rift system: geochemical evidence from the Kivu volcanic province. Lithos 48, 237–262.
Gao, S., Rudnick, R.L., Yuan, H., Liu, X., Liu, Y., Xu, W., Ling, W., Ayers, J., Wang, X., Wang, Q., 2004. Recycling lower continental crust in the North China craton. Nature 432, 892–897.
Gao, Y.F., Yang, Z.S., Santosh, M., Hou, Z.Q., Wei, R.H., Tian, S.H., 2010. Adakitic rocks from slab melt-modified mantle sources in the continental collision zone of southern Tibet. Lithos 119, 651–663.
Gao, L.Z., Zhang, C.H., Yin, C.Y., Shi, X.Y., Wang, Z.Q., Liu, Y.M., Liu, P., Tang, F., Song, B., 2008. SHRIMP zircon ages: Basis for refining the chronostratigraphic classification of the Meso- and Neoproterozoic strata in North China old land. Acta Geosci. Sin. 29, 366–376 (in Chinese with English abstract).
Gibson, S.A., Thompson, R.N., Leonardos, O.H., Dickin, A.P., Mitchell, J.G., 1995. The late Cretaceous impact of the Trindade mantle plume: evidence from large-volume, mafic, potassic magmatism in SE Brazil. J. Petrol. 36, 189–229.

Griffin, W.L., Zhang, A., O'Reilly, S.Y., Ryan, C.G., 1998. Phanerozoic evolution of the lithosphere beneath the Sino-Korean Craton. In: Flower, M.F.J., Chung, S.L., Lo, C. H., Lee, T.Y. (Eds.), Mantle dynamics and plate interaction in East Asia. American Geophysical Union, Geodynamics Series, 27, 107–126.
Griffin, W.L., Ryan, C.G., Kaminsky, F.V., O'Reilly, S.Y., Natapov, L.M., Win, T.T., Kinny, P.D., Ilupin, I.P., 1999. The Siberian lithosphere traverse: mantle terranes and the assembly of the Siberian Craton. Tectonophysics 310, 1–35.
Griffin, W.L., Jackson, S.E., Pearson, N.J., O'Reilly, S.Y., 2002. Zircon geochemistry and magma mixing, SE China: in-situ analysis of Hf isotopes, Tonglu and Pingtan igneous complexes. Lithos 61, 237–269.
Griffin, W.L., Pearson, N.J., Belousova, E.A., O'Reilly, S.Y., van Achterberg, E., Shee, S. R., 2000. The Hf isotope composition of cratonic mantle: LAM–MC–ICPMS analysis of zircon megacrysts in kimberlites. Geochim. Cosmochim. Acta. 64, 133–147.
Hanchar, J.M., Rudnick, R.L., 1995. Revealing hidden structures: the application of cathodoluminescence and back-scattered electron imaging to dating zircons from lower crustal xenoliths. Lithos 36, 289–303.
Handley, H.K., Turner, S.P., Smith, I.E., Stewart, R.B., Cronin, S.J., 2008. Rapid timescales of differentiation and evidence for crustal contamination at intra-oceanic arcs: geochemical and U–Th–Ra–Sr–Nd isotopic constraints from Lopevi Volcano, Vanuatu, SW Pacific. Earth Planet. Sci. Lett. 273, 184–194.
HBGMR (Hebei Bureau of Geology and Mineral Resources), 1989, Regional Geology of Hebei Province, Beijing Municipality and Tianjin Municipality: Beijing, Geological Publishing House, 741 (in Chinese with English abstract).
Hirth, G., Evans, R.L., Chave, A.D., 2000. Comparison of continental and oceanic mantle electrical conductivity: is the Archean lithosphere dry? Geochem. Geophys. Geosyst. 1, 12.
Hoskin, P.W.O., 2001. Patterns of chaos: fractal statistics and the oscillatory chemistry of zircon. Geochim. Cosmochim. Acta. 64, 1905–1923.
Hoskin, P.W.O., Black, L.P., 2000. Metamorphic zircon formation by solid state recrystallization of protolith igneous zircon. J. Metamorph. Geol. 18, 423–439.
Hou, K.J., Li, Y.H., Zou, T.R., Qu, X.M., Shi, Y.R., Xie, G.Q., 2007. Laser ablation–MC–ICPMS technique for Hf isotope microanalysis of zircon and its geological applications. Acta Petrol. Sin. 23, 2595–2604 (in Chinese with English abstract).
Howarth, G.H., Barry, P.H., Pernet-Fisher, J.F., Baziotis, I.P., Pokhilenko, N.P., Pokhilenko, L.N., Bodnar, R.J., Taylor, L.A., Agashev, A.M., 2014. Superplume metasomatism: evidence from Siberian mantle xenoliths. Lithos 184–187, 209–224.
Ionov, D.A., Griffin, W.L., Oreilly, S.Y., 1997. Volatile-bearing minerals and lithophile trace elements in the upper mantle. Chem. Geol. 141, 153–184.
Irvine, T.H., Baragar, W.R.A., 1971. A guide to the chemical classification of the common volcanic rocks. Can. J. Earth Sci. 8, 523–548.
Jahn, B.M., Liu, D., Wan, Y., Song, B., Wu, J., 2008. Archean crustal evolution of the Jiaodong Peninsula, China, as revealed by zircon SHRIMP geochronology, elemental and Nd-isotope geochemistry. Am. J. Sci. 308, 232–269.
Ji, Z.J., Zhang, Z.C., Han, B.F., Yu, H.F., Chen, Y., 2017. Zircon U–Pb–Hf isotopes and geochemistry analyses of the Huyu igneous rocks in northwestern Beijing, China: possible new evidence for the initial destruction of the North China Craton. Int. Geol. Rev. 60, 196–216.
Jing, W.S., Guan, A.l., 1999. Isotopic age of the Archean rocks in Beijing Area and their geological implications. Prog. Precambr. Res. 13, 1–13 (in Chinese with English abstract).
Johnson, M.C., Plank, T., 2000. Dehydration and melting experiments constrain the fate of subducted sediments. Geochem. Geophys. Geosyst. 1, 12.
Jordan, T.H., 1975. The continental tectosphere. Rev. Geophys. Space Phys. 13, 1–12.
Kemp, A.I.S., Hawkesworth, C.J., 2006. Using hafnium and oxygen isotopes in zircons to unravel the record of crustal evolution. Chem. Geol. 226, 144–162.
Klemme, S., O'Neill, H.S., 2000. The near-solidus transition from garnet lherzolite to spinel lherzolite. Contrib. Mineral. Petr. 138, 237–248.
Koglin, N., Kostopoulos, D., Reischmann, T., 2009. The Lesvos mafic–ultramafic complex, Greece: ophiolite or incipient rift? Lithos 108, 243–261.
La Flèche, M.R., Camiré, G., Jenner, G.A., 1998. Geochemistry of post-Acadian, Carboniferous continental intraplate basalts from the Maritimes Basin, Magdalen Islands, Québec. Canada. Chem. Geol. 148, 115–136.
LaTourrette, T., Hervig, R.L., Holloway, J.R., 1995. Trace element partitioning between amphibole, phlogopite, and basanite melt. Earth Planet. Sci. Lett. 135, 13–30.
Le Maitre, R.W., 2002. Igneous Rocks: a Classification and Glossary of Terms: Recommendations of the International Union of Geological Sciences Subcommission on the Systematics of Igneous Rocks. Cambridge Univ. Press, Cambridge.
Lee, C.T., Yin, Q.Z., Rudnick, R.L., Chesley, J.T., Jacobsen, S.B., 2000. Osmium isotopic evidence for Mesozoic removal of lithospheric mantle beneath the Sierra Nevada, California. Science 289, 1912–1916.
Li, Z., Chen, B., 2014. Geochronology and geochemistry of the Paleoproterozoic meta-basalts from the Jiao–Liao–Ji Belt, North China Craton: implications for petrogenesis and tectonic setting. Precambr. Res. 255, 653–676.
Li, Z., Chen, B., Wang, J.L., 2016a. Geochronological framework and geodynamic implications of mafic magmatism in the Liaodong Peninsula and adjacent regions, North China Craton. Acta Geol. Sin. (Engl. Ed.) 90, 138–153.
Li, Z., Chen, B., Wei, C.J., 2016b. Hadean detrital zircon in the North China Craton. J. Mineral. Petrol. Sci. 111, 283–291.
Li, Z., Chen, B., 2019. Lithotectonic elements of Archean basement on the Liaodong Peninsula and its vicinity, North China Craton. Front Earth Sci. Chin. 13, 209–228.
Li, X.H., Li, Z.X., Wingate, M.T.D., Chung, S.L., Liu, Y., Lin, G.C., Li, W.X., 2006. Geochemistry of the 755 Ma Mundine Well dyke swarm, northwestern Australia: part of a Neoproterozoic mantle superplume beneath Rodinia? Precambrian Res. 146, 1–15.
Li, S.R., Santosh, M., 2014. Metallogeny and craton destruction: records from the North China Craton. Ore Geol. Rev. 56, 376–414.
Li, Z., Wei, C.J., 2017. Two Types of Neoarchean basalts from Qingyuan greenstone belt, North China Craton: petrogenesis and tectonic implications. Precambr. Res. 292, 175–193.
Li, Z., Wei, C.J., Zhang, S.W., Yang, C., Duan, Z.Z., 2019. Neoarchean granitoid gneisses in Eastern Hebei, North China Craton: Revisited. Precambr. Res. 324, 62–85.
Li, Z., Wei, C.J., Chen, B., Fu, B., Gong, M.Y., 2020. Late Neoarchean reworking of the Mesoarchean crustal remnant in northern Liaoning, North China Craton: a U–Pb–Hf–O–Nd perspective. Gondwana Res. 80, 350–369.
Li, Z., Wei, C.J., Chen, B., Yang, F., Zhang, X., Cui, Y., 2022. Late Neoarchean high-grade regional metamorphism in the eastern North China Craton: New constraints from monazite dating in northern Liaoning. Precambrian Res 373, 106625.
Li, Z., Wei, C.J., Chen, B., Zhang, W., Yang, F., 2021b. U–Pb–Hf–O–Nd isotopic and geochemical constraints on the origin of Archean TTG gneisses from North China Craton: implications for crustal growth. Precambr. Res. 354, 106078.
Li, Z., Wei, C.J., Yang, C., Zhang, X., 2024. A deep mantle source for the Late Neoarchean metamorphosed basalts in Eastern Hebei, North China Craton: insights from whole-rock geochemistry and Sm–Nd isotopes, and zircon U–Pb–Hf isotopes. J. Earth Sci. 35, 29–40.
Li, W.K., Yang, Z.M., Chiaradia, M., Zhou, L., Hou, Z., 2021a. Enrichment nature of ultrapotassic rocks in southern Tibet inherited from their mantle source. J. Petrol. 62, egab060.
Liou, P., Guo, J.H., Huang, G.Y., Fan, W.B., 2019. 2.9 Ga magmatism in Eastern Hebei, North China Craton. Precambr. Res. 326, 6–23.
Liu, J.G., Cai, R.H., Pearson, D.G., Scott, J.M., 2019. Thinning and destruction of the lithospheric mantle root beneath the North China Craton: a review. Earth Sci. Rev. 196, 102873.
Liu, F.L., Liu, P.H., Ding, Z.J., Liu, J.H., Yang, H., Hu, W.H., 2012. Genetic mechanism of granitic leucosome within high-pressure granulite from the Early Precambrian metamorphic basement of Shandong Peninsula, SE North China Craton. Acta Petrol. Sin. 28, 2686–2696 (in Chinese with English abstract).
Liu, D.Y., Wilde, S.A., Wan, Y.S., Wu, J.S., Zhou, H.Y., Dong, C.Y., Yin, X.Y., 2008. New U–Pb and Hf isotopic data confirm Anshan as the oldest preserved segment of the North China Craton. Am. J. Sci. 308, 200–231.
Liu, D.Y., Wilde, S.A., Wan, Y.S., Wang, S.Y., Valley, J.W., Kita, N., Dong, C.Y., Xie, H.Q., Yang, C.X., Zhang, Y.X., Gao, L.Z., 2009. Combined U–Pb, hafnium and oxygen isotope analysis of zircons from meta-igneous rocks in the southern North China Craton reveal multiple events in the Late Mesoarchean-Early Neoarchean. Chem. Geol. 261, 140–154.
Liu, D., Zhao, Z., Zhu, D., Niu, Y., DePaolo, D.J., Harrison, T.M., Mo, X., Dong, G., Zhou, S., Sun, C., Zhang, Z., Liu, J., 2014. Postcollisional potassic and ultrapotassic rocks in southern Tibet: mantle and crustal origins in response to India-Asia collision and convergence. Geochim. Cosmochim. Acta 143, 207–231.
Lu, S.N., Zhao, G.C., Wang, H.C., Han, G., 2008. Precambrian metamorphic basement and sedimentary cover of the North China Craton: a review. Precambr. Res. 160, 77–93.
Ludwig, K.R., 2003. ISOPLOT 3: a geochronological toolkit for Microsoft Excel. Berkeley Geochronology Centre Special Publication 4, 37–41.
Luhr, J.F., 1997. Extensional tectonics and the diverse primitive volcanic rocks in the western Mexican Volcanic Belt. Can. Mineral. 35, 473–500.
Luhr, J.F., Allan, J.F., Carmichael, I.S.E., Nelson, S.A., Hasenaka, T., 1989. Primitive calc-alkaline and alkaline rock types from the western Mexican Volcanic Belt. J. Geophys. Res. 94, 4515–4530.
Ma, L., Jiang, S.Y., Hou, M.L., Dai, B.Z., Jiang, Y.H., Yang, T., Zhoa, K.D., Pu, W., Zhu, Z. Y., Xu, B., 2014. Geochemistry of Early Cretaceous calc-alkaline lamprophyres in the Jiaodong Peninsula: implication for lithospheric evolution of the eastern North China Craton. Gondwana Res. 25, 859–872.
Manley, C.R., Glazner, A.F., Farmer, G.L., 2000. Timing of volcanism in the Sierra Nevada of California: evidence for the Pliocene delamination of the batholithic root? Geology 28, 811–814.
Mao, J.W., Wang, Y.T., Zhang, Z.H., Yu, J.J., Niu, B.G., 2003. Geodynamic settings of Mesozoic large-scale mineralization in North China and adjacent areas: implication from the highly precise and accurate ages of metal deposits. Sci. China Earth Sci. 46, 838–851.
Mao, J.W., Xie, G.Q., Zhang, Z.H., Li, X.F., Wang, Y.T., Zhang, C.Q., Li, Y.F., 2005. Mesozoic large-scale metallogenic pulses in North China and corresponding geodynamic setting. Acta Petrol. Sin. 21, 169–188 (in Chinese with English abstract).
McKenzie, D.P., 1989. Some remarks on the movement of small melt fractions in the mantle. Earth Planet. Sci. Lett. 95, 53–72.
McKenzie, D.P., Bickle, M.J., 1988. The volume and composition of melt generated by extension of the lithosphere. J. Petrol. 29, 625–679.
Meng, Q.R., Wu, G.L., Fan, L.G., Wei, H.H., Wang, E., 2020. Late Triassic uplift, magmatism and extension of the northern North China block: mantle signatures in the surface. Earth Planet. Sci. Lett. 547, 116451.
Menzies, D.P., 1989. Some remarks on the movement of small melt fractions in the mantle. Earth Planet. Sci. Lett. 95, 53–72.
Menzies, A., Fan, W.M., Zhang, M., 1993. Paleozoic and Cenozoic lithoprobes and the loss of >120 km of Archean lithosphere, Sino-Korean craton, China. In: Prichard, H. M., et al. (Ed.), Magmatic processes and plate tectonics. Geol. Soc., Spec. Publ, London 76, 71–81.
Menzies, M., Xu, Y.G., Zhang, H.F., Fan, W.M., 2007. Integration of geology, geophysics, and geochemistry: a key to understanding the North China Craton. Lithos 96, 1–21.
Middlemost, E.A., 1994. Naming materials in the magma/igneous rock system. Earth Sci. Rev. 37, 215–224.

Miller, C., Schuster, R., Klotzli, U., Frank, W., Purtscheller, F., 1999. Post-collisional potassic and ultrapotassic magmatism in SW Tibet: geochemical and Sr–Nd–Pb–O isotopic constraints for mantle source characteristics and petrogenesis. J. Petrol. 40, 1399–1424.
Niu, X.L., Chen, B., Feng, G.Y., Liu, F., Yang, J.S., 2017. Origin of lamprophyres from the northern margin of the North China Craton: implications for mantle metasomatism. J. Geol. Soc. London 174, 353–364.
Niu, Y., O'Hara, M.J., 2008. Global correlations of ocean ridge basalt chemistry with axial depth: a new perspective. J. Petrol. 49, 633–664.
Owen, J.P., 2008. Geochemistry of lamprophyres from the Western Alps, Italy: implications for the origin of an enriched isotopic component in the Italian mantle. Contrib. Mineral. Petr. 155, 341–362.
Pearce, J.A., 2008. Geochemical fingerprinting of oceanic basalts with applications to ophiolite classification and the search for Archean oceanic crust. Lithos 100, 14–48.
Pearce, J.A., Peate, D.W., 1995. Tectonic implications of the composition of volcanic arc magmas. Annu. Rev. Earth Planet. Sci. 23, 251–285.
Pearce, J.A., Stern, R.J., Bloomer, S.H., Fryer, P., 2005. Geochemical mapping of the Mariana arc-basin system: implications for the nature and distribution of subduction components. Geochem. Geophy. Geosy. 6, Q07006.
Peng, P., Zhai, M.G., Su, X.D., Zhao, T.P., Zhou, Y.Y., 2017. Nature of the Late Carboniferous to Triassic magmatism along the northern margin of the North China block: link with the evolution of the Central Asian Orogen. Geodyn. Tectonophys. 8, 531532.
Plank, T., 2005. Constraints from Thorium/Lanthanum on sediment recycling at subduction zones and the evolution of the continents. J. Petrol. 46, 921–944.
Prelević, D., Foley, S.F., Cvetković, V., 2012. A review of petrogenesis of Mediterranean Tertiary lamproites: A perspective from the Serbian ultrapotassic province. In: Beccaluva, L., Bianchini, G., Wilson, M. (Eds.) Cenozoic Volcanism in the Mediterranean Area. Geol. Soc. Am. Spec. Papers 418, 113–129.
Prelević, D., Foley, S.F., Romer, R., Conticelli, S., 2004. Origin of minette by mixing of lamproite and dacite magmas in Veliki Majdan. Serbia. J. Petrol. 45, 759–792.
Prelević, D., Foley, S.F., Romer, R., Conticelli, S., 2008. Mediterranean Tertiary lamproites derived from multiple source components in postcollisional geodynamics. Geochim. Cosmochim. Ac. 72, 2125–2156.
Pupin, J.P., 1980. Zircon and granite petrology. Contrib. Mineral. Petr. 73, 207–220.
Read, G., Grutter, H., Winter, S., Luckman, N., Gaunt, F., Thompsen, F., 2004. Stratigraphic relations, kimberlite emplacement and lithospheric thermal evolution, Quirico Basin, Minas Gerais State, Brazil. Lithos 77, 803–818.
Ren, R., Han, B.F., Zhang, Z.C., Li, J.F., Yang, Y.H., Zhang, Y.B., 2011. Zircon U–Pb and Hf isotopic studies of basement gneiss and overlying Meso-Neoproterozoic sedimentary rocks from the Changping area, Beijing, and their geological implications. Acta Petrol. Sin. 27, 1721–1745 (in Chinese with English abstract).
Rock, N.M.S., 1987. The nature and origin of lamprophyres: an overview. In: Fitton, J.G., Upton, B.G. (Eds.), Geol. Soc., Spec. Publ, London 30, pp. 191–226. The Alkaline Igneous Rocks.
Rudnick, R.L., Gao, S., 2003. The composition of the continental crust. In: Rudnick, R.L. (Ed.), The Crust. Elsevier-Pergamon, Oxford, pp. 1–64.
Scherer, E., Münker, C., Mezger, K., 2001. Calibration of the lutetium-hafnium clock. Science 293, 683–687.
Smith, E.I., Sanchez, A., Walker, J.D., Wang, K., 1999. Geochemistry of mafic magmas in the Hurricane Volcanic field, Utah: implications for small-and large-scale chemical variability of the lithospheric mantle. Geology 107, 433–448.
Song, S.G., Niu, Y.L., Wei, C.J., Ji, J.Q., Su, L., 2010. Metamorphism, anatexis, zircon ages and tectonic evolution of the Gongshan block in the northern Indochina continent-an eastern extension of the Lhasa block. Lithos 120, 327–346.
Song, B., Nutman, A.P., Liu, D.Y., Wu, J.S., 1996. 3800–2500 Ma crust in the Anshan area of Liaoning Province, northeastern China. Precambrian Res. 78, 79–94.
Spath, A., Le Roex, A.P., Duncan, R.A., 1996. The geochemistry of lavas from the Comores Archipelago, western Indian Ocean: petrogenesis and mantle source region characteristics. J. Petrol. 37, 961–991.
Stracke, A., 2012. Earth's heterogeneous mantle: a product of convection-driven interaction between crust and mantle. Chem. Geol. 330, 274–299.
Su, X.D., Peng, P., Wang, C., Sun, F.B., Zhang, Z.Y., Zhou, X.T., 2018. Petrogenesis of a ~900 Ma mafic sill from Xuzhou, North China: implications for the genesis of Fe–Ti–rich rocks. Lithos 318–319, 357–375.
Sun, S.S., McDonough, W.F., 1989. Chemical and isotopic systematics of oceanic basalts: implications for mantle composition and processes. In: Saunders, A.D., Norry, M.J. (Eds.), Magmatism in the Ocean Basins. Geol. Soc., 42. Spec. Publ, London, pp. 313–345.
Tappe, S., Foley, S.E., Stracke, A., Romer, R.L., Kjarsgaard, B.A., Heaman, L.M., Joyce, N., 2007. Craton reactivation on the Labrador Sea margins: $^{40}Ar/^{39}Ar$ age and Sr–Nd–Hf–Pb isotope constraints from alkaline and carbonatite intrusives. Earth Planet. Sci. Lett. 256, 433–454.
Taylor, S.R., McLennan, S.M., 1995. The geochemical composition of the continental crust. Rev. Geophys. 33, 241–265.
Thompson, R.N., Leat, P.T., Dickin, A.P., Hendry, M.A., Gibson, S.A., 1990. Strongly potassic mafic magmas from lithospheric mantle sources during continental extension and heating: evidence from Miocene minettes of northwest Colorado, U.S.A. Earth Planet. Sci. Lett. 98, 139–153.
Tian, W., Chen, B., Liu, C.Q., Zhang, H.F., 2007, Zircon U–Pb age and Hf isotopic composition of the Xiaozhangjiakou ultramafic pluton in north Hebei: Acta Petrol. Sin. 23, 583–590 (in Chinese with English abstract).
Tommasini, S., Avanzinelli, R., Conticelli, S., 2011. The Th/La and Sm/La conundrum of the Tethyan realm lamproites. Earth Planet. Sci. Lett. 301, 469–478.
Vervoort, J.D., Plank, T., Prytulak, J., 2011. The Hf–Nd isotopic composition of marine sediments. Geochim. Cosmochim. Ac. 75, 5903–5926.
Wan, Y.S., Liu, D.Y., Song, B., Wu, J.S., Yang, C.H., Zhang, Z.Q., Geng, Y.S., 2005. Geochemical and Nd isotopic compositions of 3.8 Ga meta-quartz dioritic and trondhjemitic rocks from the Anshan area and their geological significance. J. Asian Earth Sci. 24, 563–575.
Wan, Y.S., Liu, D.Y., Yin, X.Y., Wu, J.S., Wilde, S.A., 2007. SHRIMP geochronology and Hf isotope composition of zircons from the Tiejiashan granite and supracrustal rocks in the Anshan area Liaoning province. Acta Petrol. Sin. 23, 241–252 (in Chinese with English abstract).
Wan, Y.S., Liu, D.Y., Wang, S.J., Yang, E.X., Wang, W., Dong, C.Y., Zhou, H.Y., Du, L.L., Yang, Y.H., Diwu, C.R., 2011. ~2.7 Ga juvenile crust formation in the North ChinaCraton (Taishan–Xintai area, western Shandong Province): further evidence of an understated event from zircon U–Pb dating and Hf isotope composition. Precambr. Res. 186, 169–180.
Wan, Y.S., Liu, D.Y., Nutman, A.P., Zhou, H.Y., Dong, C.Y., Yin, X.Y., Ma, M.Z., 2012a. Multiple 3.8–3.1 Ga tectono-magmatic events in a newly discovered area of ancient rocks (the Shengousi Complex), Anshan, North China Craton. J. Asian Earth Sci. 54–55, 18–30.
Wan, Y.S., Wang, S.J., Liu, D.Y., Wang, W., Kröner, A., Dong, C.Y., Yang, E.X., Zhou, H.Y., Xie, H.Q., Ma, M.Z., 2012b. Redefinition of depositional ages of Neoarchean supracrustal rocks in western Shandong Province, China: SHRIMP U–Pb zircon dating. Gondwana Res. 768–784.
Wallace, P., Carmichael, I.S.E., Righte, K., Becker, T.A., 1992. Volcanism and tectonism in western Mexico: a contrast of style and substance. Geology 20, 625–628.
Wan, Y.S., Liu, D.Y., Dong, C.Y., Xie, H.Q., Kröner, A., Ma, M.Z., Liu, S.J., Xie, S.W., Ren, P., 2015. Formation and evolution of Archean continental crust of the North China Craton. Precambrian Geology of China. Springer Geol. 59–136.
Wan, T.F., Zhao, Q.L., 2012. The genesis of tectono-magmatism in eastern China. Sci. China Earth Sci. 55, 347–354.
Wang, Y., Fan, W., Peng, T., Zhang, H., Guo, F., 2005. Nature of the Mesozoic lithospheric mantle and tectonic decoupling beneath the Dabie Orogen, Central China: evidence from $^{40}Ar/^{39}Ar$ geochronology, elemental and Sr–Nd–Pb isotopic compositions of early Cretaceous mafic igneous rocks. Chem. Geol. 220, 165–189.
Wang, H.Z., Mo, X.X., 1996. An outline of the tectonic evolution of China. Episodes 18, 6–16.
Wang, C., Song, S.G., Su, L., Allen, M.B., Dong, J.L., 2021. Lithospheric modification at the onset of the destruction of the North China Craton: evidence from Late Triassic mafic dykes. Chem. Geol. 566, 120105.
Willbold, M., Stracke, A., 2006. Trace element composition of mantle end-members: Implications for recycling of oceanic and upper and lower continental crust. Geochem. Geophy. Geosy. 7, 4.
Willbold, M., Stracke, A., 2010. Formation of enriched mantle components by recycling of upper and lower continental crust. Chem. Geol. 276, 188–197.
Wilson, M., Downes, H., 1991. Tertiary Quaternary extension-related alkaline magmatism in western and central-Europe. J. Petrol. 32, 811–849.
Windley, B.F., Alexelev, D., Xiao, W.J., Kröner, A., Badarch, G., 2007. Tectonic models for accretion of the Central Asian Orogenic Belt. J. Geol. Soc. London 164, 31–47.
Wu, F.Y., Walker, R.J., Ren, X.W., Sun, D.Y., Zhou, X.H., 2003. Osmium isotopic constraints on the age of lithospheric mantle beneath northeastern China. Chem. Geol. 196, 107–129.
Wu, F.Y., Yang, J.H., Liu, X.M., 2005a. Geochronological framework of the Mesozoic granitic magmatism in the Liaodong Peninsula, Northeast China. Geol. J. China Univ. 11, 305–317 (in Chinese with English abstract).
Wu, F.Y., Lin, J.Q., Wilde, S.A., Zhang, X.O., Yang, J.H., 2005b. Nature and significance of the Early Cretaceous giant igneous event in Eastern China. Earth Planet. Sci. Lett. 233, 103–119.
Wu, F.Y., Walker, R.J., Yang, Y.H., Yuan, H.L., Yang, J.H., 2006a. The chemical-temporal evolution of lithospheric mantle underlying the North China Craton. Geochim. Cosmochim. Ac. 70, 5013–5034.
Wu, F.Y., Yang, Y.H., Xie, L.W., Yang, J.H., Xu, P., 2006b. Hf isotopic compositions of the standard zircons in U–Pb geochronology. Chem. Geol. 234, 105–126.
Wu, F.Y., Li, X.H., Yang, J.H., Zheng, Y.F., 2007. Discussion on the petrogenesis of granites. Acta Petrol. Sin. 23, 1217–1238 (in Chinese with English abstract).
Wu, F.Y., Xu, Y.G., Gao, S., Zheng, J.P., 2008. Lithospheric thinning and destruction of the North China Craton. Acta Petrol. Sin. 24, 1145–1174 (in Chinese with English abstract).
Wu, F.Y., Yang, Y.H., Xu, Y.G., Wilde, S.A., Walker, R.J., 2019. Destruction of the North China Craton in the Mesozoic. Annu. Rev. Earth Pl. Sc. 47, 173–195.
Wu, Y.D., Yang, J.H., Wang, H., Zhu, Y.S., Xu, L., Zhou, B.Q., Li, R., 2021. Origin and tectonic implications of Early Cretaceous Siziwangqi volcanic rocks from the North China Craton. Lithos 400–401, 106431.
Wu, M., Zhao, G., Sun, M., Li, S., He, Y., Bao, Z., 2013. Zircon U–Pb geochronology and Hf isotopes of major lithologies from the Yishui Terrane: implications for the crustal evolution of the Eastern Block, North China Craton. Lithos 170–171, 164–178.
Wu, M., Zhao, G., Sun, M., Li, S., 2014. A synthesis of geochemistry and Sm–Nd isotopes of Archean granitoid gneisses in the Jiaodong Terrane: constraints on petrogenesis and tectonic evolution of the Eastern Block, North China Craton. Precambr. Res. 255, 885–899.
Xiao, W.J., Han, F.L., Windley, B.F., Yuan, C., Zhou, H., Li, J.L., 2003. Multiple accretionary orogenies and episodic growth of continents: insights from the Western Kunlun Range, central Asia. Int. Geol. Rev. 45, 303–328.
Xie, S., Xie, H., Wang, S., Kröner, A., Liu, S., Zhou, H., Ma, M., Dong, C., Liu, D., Wan, Y., 2014. Ca. 2.9 Ga granitoid magmatism in eastern Shandong, North China Craton: Zircon dating, Hf–in–zircon isotopic analysis and whole-rock geochemistry. Precambrian Res. 255, 538–562.

Xu, Y.G., 2001. Thermo-tectonic destruction of the Archean lithospheric keel beneath eastern China: evidence, timing and mechanism. Phys. Chem. Earth Part a. 26, 747–757.
Xu, Y.G., Huang, X., Ma, J., Wang, Y., Iizuka, Y., Xu, J., Wang, Q., Wu, X., 2004. Crust-mantle interaction during the tectono-thermal reactivation of the North China Craton: constraints from SHRIMP zircon U–Pb chronology and geochemistry of Mesozoic plutons from western Shandong. Contrib. Mineral. Petr. 147, 750–767.
Xu, Y.G., Li, H.Y., Pang, C.J., He, B., 2009. On the timing and duration of the destruction of the North China Craton. Chin. Sci. Bull. 54, 3379–3396.
Xu, Y.G., Li, H.Y., Hong, L.B., Ma, L., Ma, Q., Sun, M.D., 2018. Generation of Cenozoic intraplate basalts in the big mantle wedge under eastern Asia. Sci. China Earth Sci. 61, 869–886.
Yang, Z.Y., Jiang, S.Y., 2018. Diverse lamprophyres origins corresponding to lithospheric thinning: a case study in the Jiurui district of Middle-lower Yangtze River Belt, South China Craton. Gondwana Res. 54, 62–80.
Yang, J.H., Wu, F.Y., Wilde, S.A., 2003. A review of the geodynamic setting of large-scale Late Mesozoic gold mineralization in the North China Craton: an association with lithospheric thinning. Ore Geol. Rev. 23, 125–152.
Yang, J.H., Wu, F.Y., Chung, S.L., Wilde, S.A., Chu, M.F., 2004. Multiple sources for the origin of granites: geochemical and Nd/Sr isotopic evidence from the Gudaoling granite and its mafic enclaves, northeast China. Geochim. Cosmochim. Ac. 68, 4469–4483.
Yang, J.H., Wu, F.Y., Shao, J.A., Wilde, S.A., Xie, L.W., Liu, X.M., 2006. Constraints on the timing of uplift of the Yanshan Fold and Thrust Belt. North China. Earth Planet. Sci. Lett. 246, 336–352.
Yang, J.H., Wu, F.Y., Chung, S.L., Lo, C.H., Wilde, S.A., Davis, G.A., 2007a. Rapid exhumation and cooling of the Liaonan metamorphic core complex inferred from $^{40}Ar/^{39}Ar$ thermochronology: implications for the Late Mesozoic tectonic evolution of North China craton. Geol. Soc. Am. Bull. 119, 1405–1414.
Yang, J.H., Wu, F.Y., Wilde, S.A., Liu, X.M., 2007b. Petrogenesis of Late Triassic granitoids and their enclaves with implications for post-collisional lithospheric thinning of the Liaodong Peninsula, North China Craton. Chem. Geol. 242, 155–175.
Yang, J.H., Wu, F.Y., Liu, X.M., Xie, L.W., Yang, Y.H., 2007c. Petrogenesis and geological significance of the Jurassic Xiaoheishan pluton in the Liaodong Peninsula, east China: in-situ zircon U–Pb dating and Hf isotopic analysis. Bull. Mineral. Petrol. Geochem. 26, 29–43 (in Chinese with English abstract).
Yang, J.H., Sun, J.F., Chen, F., Wilde, S.A., Wu, F.Y., 2007d. Sources and petrogenesis of Late Triassic dolerite dikes in the Liaodong Peninsula: Implications for post-collisional lithosphere thinning of the eastern North China Craton. J. Petrol. 48, 1973–1997.
Yang, J.H., Wu, F.Y., Wilde, S.A., Belousova, E., Griffin, W.L., 2008a. Mesozoic decratonization of the North China block. Geology 36, 467–470.
Yang, J.H., Wu, F.Y., Wilde, S.A., Zhao, G.C., 2008b. Petrogenesis and geodynamics of Late Archean magmatism in eastern Hebei, eastern North China Craton: geochronological, geochemical and Nd–Hf isotopic evidence. Precambrian Res. 167, 125–149.
Yang, Y.H., Wu, F.Y., Wilde, S.A., Liu, X.M., Zhang, Y.B., Xie, L.W., Yang, J.H., 2009. In situ perovskite Sr–Nd isotopic constraints on the petrogenesis of the Ordovician Mengyin kimberlites in the North China Craton. Chem. Geol. 264, 24–42.
Yang, J.H., Wu, F.Y., 2009. Triassic magmatism and its relation to decratonization in the eastern North China Craton. Sci. China Earth Sci. 52, 1319–1330.
Zhai, M.G., Santosh, M., 2011. The early Precambrian odyssey of the North China Craton: a synoptic overview. Gondwana Res. 20, 6–25.
Zhai, M.G., Santosh, M., 2013. Metallogeny of the North China Craton: Link with secular changes in the evolving Earth. Gondwana Res. 24, 275–297.
Zhang, C.H., Li, C.M., Deng, H.L., Liu, Y., Liu, L., Wei, B., Li, H.B., Liu, Z., 2011. Mesozoic contraction deformation in the Yanshan and northern Taihang mountains and its implications to the destruction of the North China Craton. Sci. China Earth Sci. 54, 798–822.
Zhang, S.T., Long, X.P., Zhang, F.Y., Zhang, L., 2023. Transcrustal magma plumbing process in the Cenozoic Dali potassic lamprophyre dyke formation in the southeastern Tibet Plateau. Lithos 454–455, 107281.
Zhang, H.F., Sun, M., 2002. Geochemistry of Mesozoic basalts and mafic dikes, southeastern North China Craton, and tectonic implications. Int. Geol. Rev. 44, 370–382.
Zhang, H., Thurber, C.H., Shelly, D., Ide, S., Beroza, G.C., Hasegawa, A., 2003. High-resolution subducting slab structure beneath northern Honshu, Japan, revealed by double-difference tomography. Geology 32, 361–364.
Zhang, H.F., Yang, Y.H., 2007. Emplacement age and Sr–Nd–Hf isotopic characteristics of the diamondiferous kimberlites from the eastern North China Craton. Acta Petrol. Sin. 23, 285–294 (in Chinese with English abstract).
Zhang, S.H., Zhao, Y., Liu, X.C., Liu, D.Y., Chen, F., Xie, L.W., Chen, H.H., 2009a. Late Paleozoic to Early Mesozoic mafic–ultramafic complexes from the northern North China Block: constraints on the composition and evolution of the lithospheric mantle. Lithos 110, 229–246.
Zhang, S.H., Zhao, Y., Kröner, A., Liu, X.M., Xie, L.W., Chen, F.K., 2009b. Early Permian plutons from the northern North China Block: constraints on continental arc evolution and convergent margin magmatism related to the Central Asian Orogenic Belt. Int. J. Earth Sci. 98, 1441–1467.
Zhang, S.H., Zhao, Y., Sonh, B., Hu, J.M., Liu, S.W., Yang, Y.H., Chen, F.K., Liu, X.M., Liu, J., 2009c. Contrasting Late Carboniferous and Late Permian-Middle Triassic intrusive suites from the northern margin of the North China craton: Geochronology, petrogenesis, and tectonic implications. Geol. Soc. Am. Bull. 121, 181–200.
Zhang, S.H., Zhao, Y., Ye, H., Hou, K.J., Li, C.F., 2012. Early Mesozoic alkaline complexes in the northern North China Craton: implications for cratonic lithospheric destruction. Lithos 155, 1–18.
Zhang, S.H., Zhao, Y., Davis, G.A., Ye, H., Wu, F., 2014. Temporal and spatial variations of Mesozoic magmatism and deformation in the North China Craton: Implications for lithospheric thinning and decratonization. Earth Sci. Rev. 131, 49–87.
Zhao, Y., 1990. The Mesozoic orogenies and tectonic evolution of the Yanshan area. Geol. Rev. 36, 1–13 (in Chinese with English abstract).
Zhao, G.C., Kröner, A., 2007. Geochemistry of Neoarchean (ca. 2.55–2.50 ga) volcanic and ophiolitic rocks in the Wutaishan greenstone belt, central orogenic belt, North China Craton: implications for geodynamic setting and continental growth: discussion. Geol. Soc. Am. Bull. 119, 487–489.
Zhao, G.C., Zhai, M.G., 2013. Lithotectonic elements of Precambrian basement in the North China Craton: review and tectonic implications. Gondwana Res. 23, 1207–1240.
Zhao, G.C., Sun, M., Wilde, S.A., Li, S.Z., 2005. Late Archean to Paleoproterozoic evolution of the North China Craton: key issues revisited. Precambrian Res. 136, 177–202.
Zhao, J.H., Zhou, M.F., 2007. Geochemistry of Neoproterozoic mafic intrusions in the Panzhihua district (Sichuan Province, SW China): implications for subduction related metasomatism in the upper mantle. Precambrian Res. 152, 27–47.
Zheng, Y., Davis, G.A., Wang, C., Darby, B.J., Zhang, C., 2000. Major mesozoic tectonic events in the Yanshan belt and the plate tectonic setting. Acta Geol. Sin. 74, 289–302 (in Chinese with English abstract).
Zhu, R.X., Yang, Y.H., Wu, F.Y., 2012. Timing of destruction of the North China Craton. Lithos 149, 5160.